Pore texture analysis in automated 3D breast ultrasound images for implanted lightweight hernia mesh identification: a preliminary study

Jiting Yang
Department of Electronic Engineering,Yunnan University,Kunming,China
Haiyan Li
Department of Electronic Engineering,Yunnan University,Kunming,China
Jun Wu (arthandmade@qq.com)
Department of electronic engineering,Yunnan University,Kunming,China https://orcid.org/0000-0002-5944-8286
Liang Sun
Department of Gastrointestinal and Hernia Surgery,The First Affiliated Hospital of Kunming Medical University,Kunming,China
Dan Xu
Department of Electronic Engineering,Yunnan University,Kunming,China
Yuanyuan Wang
Department of Electronic Engineering,Fudan University,Shanghai,china
Yufeng Zhang
Department of Electronic Engineering,Yunnan University,Kunming,China
Yue Chen
Department of Ultrasound,Huadong Hospital,Fudan University,Shanghai,China
Lin Chen
Department of Ultrasound,Huadong Hospital,Fudan University,Shanghai,China

---

Research

Keywords: automated 3D breast ultrasound (ABUS), abdominal wall hernia, lightweight mesh, implanted mesh identification, pore texture analysis

Posted Date: December 20th, 2019

DOI: https://doi.org/10.21203/rs.2.19410/v1

Version of Record: A version of this preprint was published at BioMedical Engineering OnLine on February 25th, 2021. See the published version at https://doi.org/10.1186/s12938-021-00859-7.

Pore texture analysis in automated 3D breast ultrasound images for implanted lightweight hernia mesh identification: a preliminary study

Jiting Yang,[1,†] Haiyan Li,[1,†] Jun Wu,[1,*] Liang Sun,[2,*] Dan Xu,[1] Yuanyuan Wang,[3] Yufeng Zhang,[1] Yue Chen,[4] Lin Chen[4]

1 Department of Electronic Engineering, Yunnan University, Kunming, China
2 Department of Gastrointestinal and Hernia Surgery, The First Affiliated Hospital of Kunming Medical University, Kunming, China
3 Department of Electronic Engineering, Fudan University, Shanghai, China
4 Department of Ultrasound, Huadong Hospital, Fudan University, Shanghai, China

Corresponding author: Jun Wu, Liang Sun
*Correspondence: arthandmade@qq.com, bsunq@qq.com
†Jiting Yang and Haiyan Li contributed equally to this work

Abstract

Background: Precise visualization of meshes and their position would greatly aid in mesh shrinkage evaluation, hernia recurrence risk assessment, and the preoperative planning of salvage repair. Lightweight (LW) meshes are able to preserve abdominal wall compliance by generating less post-implant fibrosis and rigidity. However, conventional 3D imaging techniques such as computed tomography (CT) and magnetic resonance imaging (MRI) cannot visualize the LW meshes. Patients sometimes have to undergo a second-look operation for visualizing the mesh implants. The goal of this work is to investigate the potential advantages of Automated 3D breast ultrasound (ABUS) pore texture analysis for implanted LW hernia mesh identification.

Methods: In vitro, the appearances of four different flat meshes in both ABUS and 2D hand-held ultrasound (HHUS) images were evaluated and compared. In vivo, pore texture patterns of 87 hernia regions were analyzed both in ABUS images and their corresponding HHUS images.

Results: In vitro studies, the imaging results of ABUS for implanted LW meshes are much more visualized and effective in comparison to HHUS. In vivo, the inter-class distance of 40 texture features were calculated. The texture features of 2D sectional plans (axial and sagittal plane) have no significant contribution for implanted LW mesh identification. Significant contribution was observed in coronal plane. However, since the mesh may have spatial variation such as shrinkage after implant surgery, the inter-class distance of 3D coronal plane pore texture features are bigger than 2D coronal plane, so the contribution of 3D coronal plane pore texture features are more valuable than 2D coronal plane for implanted LW mesh identification. The use of 3D pore texture features significantly improved the robustness of the identification method in distinguishing the LW mesh and fascia.

Conclusions: An innovative new automated 3D breast ultrasound (ABUS) provides additional pore texture visualization, by separating the LW mesh from the fascia tissues. Therefore, ABUS having the potential to provide more accurate features to characterize pore texture patterns, and ultimately provide more accurate measures for implanted LW mesh identification.

Keywords: automated 3D breast ultrasound (ABUS), abdominal wall hernia, lightweight mesh, implanted mesh identification, pore texture analysis

Background

Repair of abdominal wall hernias is one of the most frequently performed operations across the world [1-3]. It has been estimated that 250,000 ventral hernia repairs are being done in the USA yearly [4, 5]. Today, most abdominal wall hernias are treated by placement of mesh to repair the abdominal wall defect [6-8]. Several reports have shown that compared with simple sutures, mesh is superior, with significantly reduced recurrence rates [8-11]. However, implanted mesh is a foreign body and is subject to a variety of complications, with recurrence remaining an unsolved problem and reoperation increasingly common [6, 12]. Therefore, sonologists now need perform an increasing number of examinations in patients with previously implanted meshes for either repair-related problems or other indications [1]. For evaluation of these patients, it is important to identify the mesh itself separate from the soft tissues that surround it to confirm a successful reconstruction, identify mesh failure, or better plan a salvage repair [12].

Lightweight (LW) mesh with the reduced polypropylene content and larger pore sizes between filaments has demonstrated a pronounced reduction in inflammation and improved integration into surrounding tissue in humans [13]. Based on the development tendency of minimal foreign body left behind, the heavyweight (HW) meshes are being gradually replaced by the LW meshes [14]. The previous studies showed that the LW mesh is not visible on computed tomography (CT) because it is isoattenuating relative to surrounding tissues [1, 15].

Although the 2D hand-held ultrasound (HHUS) has been shown to identify radiolucent foreign bodies[12, 16], in our experience, it has not been always reliable in identifying the LW mesh. In ventral hernia repair surgery, mesh may be placed in a variety of locations in relation to the structures of the anterior abdominal wall (Fig. 1), all of which are usually close to the fascia [8, 11]. However, in sectional views (axial and sagittal views) of HHUS, both the LW mesh and fascia are usually rendered as a linear and hyperechoic area [17]. For this reason, the texture features of HHUS images reflect mixed properties of LW mesh overlapping fascia tissues. Fascia could be considered as anatomical noise to implanted LW mesh identification, and therefore reduce the differential diagnosis value of the computed texture features.

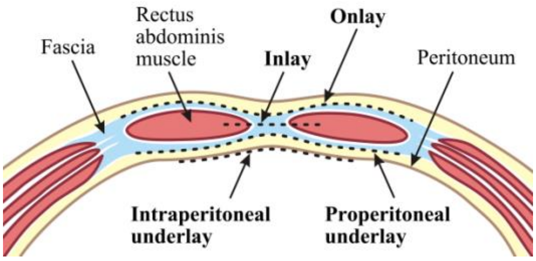

Fig. 1. Anterior abdominal wall in cross section above the arcuate line. The mesh (black dashed lines) may be anterior to the abdominal wall fascia (Onlay), be adjacent to the fascial edges (Inlay), in the preperitoneal space between the fascia and the peritoneum (Properitoneal underlay), or be attached to the peritoneum in an intraperitoneal position (Intraperitoneal underlay).

Automated 3D breast ultrasound (ABUS) is an innovative new ultrasound imaging modality in which tomographic images of the scanning area are reconstructed in 3D from a series of 2D ultrasound images that are acquired by moving a conventional transducer (Fig. 2). Clinical trials have shown that ABUS provides superior tissue visualization and improved lesion conspicuity in comparison to HHUS, resulting in higher sensitivity and specificity [18-20]. As a relatively mature 3D ultrasound modality at present, the ABUS has drawn more and more attention of scholars [21]. It is not only widely applied in breast cancer detection, but also rapidly developed in abdominal wall hernias diagnosis [22, 23]. Compared to HHUS sectional views [Fig. 3(a)], ABUS also provides additional diagnostic information from coronal views, which cannot be generated by the 2D ultrasound [18]. The new coronal plane offers superior pore texture visualization, by separating the LW mesh from the fascia tissues [Fig. 3(b-c)]. Therefore, ABUS could offer the ability to selectively analyze the texture features of the LW mesh, having the potential to provide more accurate features to characterize pore texture patterns, and ultimately provide more accurate measures for implanted LW mesh identification.

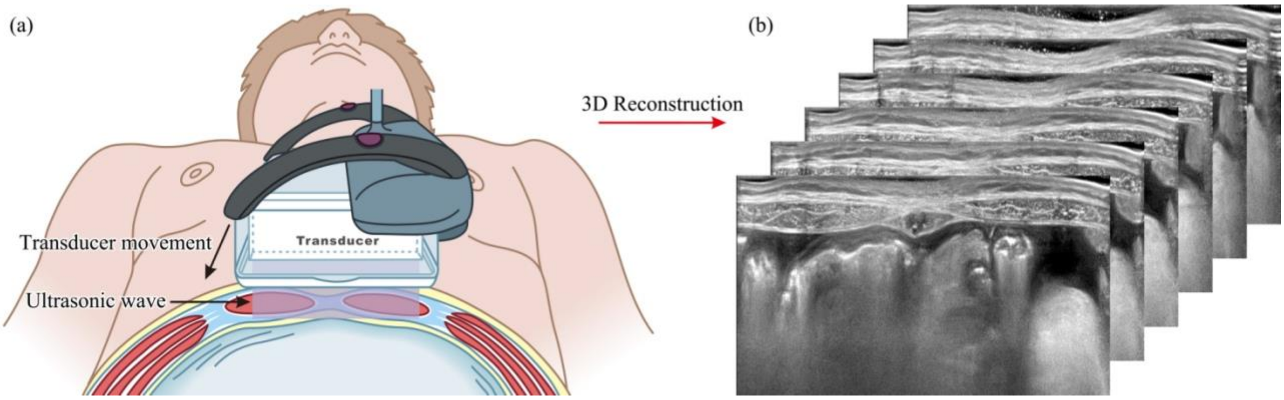

Fig. 2. An illustrative example of (a) automated 3D breast ultrasound (ABUS) acquisition geometry with (b) the reconstructed tomographic anterior abdominal wall image.

.

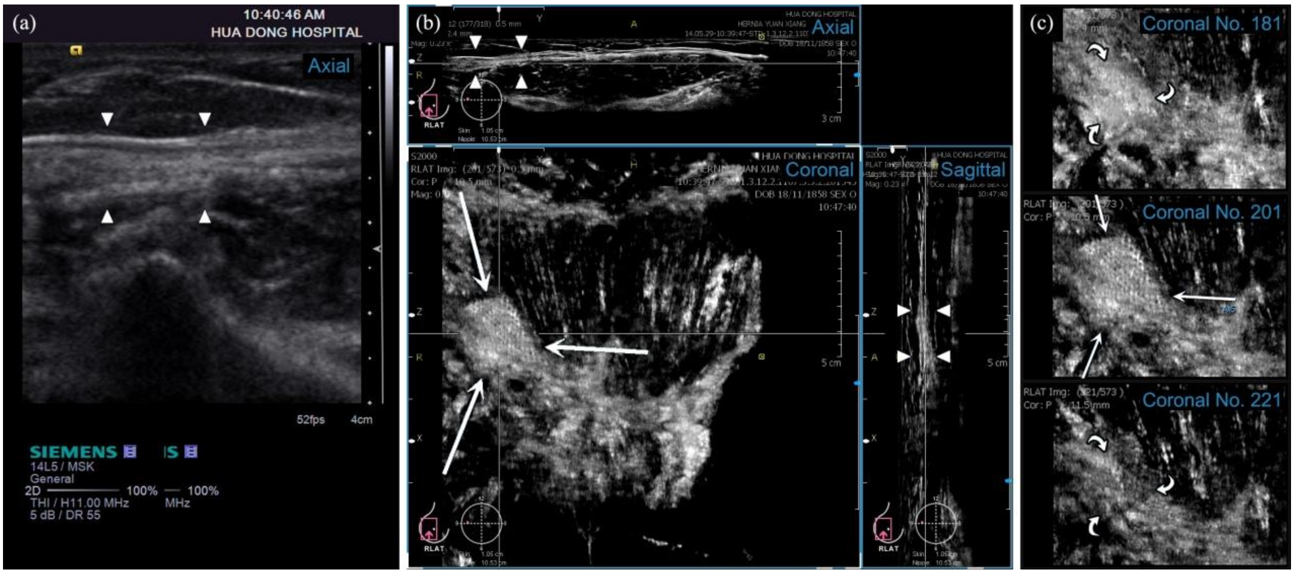

Fig. 3. Differences of texture features in (a) the axial view of HHUS, (b) the three orthogonal views of ABUS and (c) coronal multislice views of ABUS for the same LW mesh. Note that the texture features of HHUS images reflect mixed properties of LW mesh overlapping fascia tissues. Therefore, it is difficult to identify the LW mesh itself separate from the fascia tissues that surround it (arrowheads). However, the new coronal plane of ABUS offers superior pore texture visualization, by separating the LW mesh (arrows) from the fascia (curved arrows) tissues.

In this paper we present an exploratory study that investigates the potential advantages of ABUS pore texture analysis for implanted lightweight hernia mesh identification. In vitro, the appearances of four different flat meshes in both ABUS and HHUS images were evaluated and compared. In vivo, pore texture patterns of 87 hernia regions were analyzed both in ABUS images and their corresponding HHUS images. The presence of the previously implanted lightweight mesh in the hernia region was identified by using both ABUS and HHUS texture features. We compared the relative identification performance of ABUS and HHUS texture features in correlating with the established surgical findings. Although preliminary, our results suggest that ABUS pore texture analysis could potentially provide more discriminative features for implanted lightweight hernia mesh identification, in comparison to HHUS images. To the best of our knowledge, our study is the first to investigate the potential advantages of ABUS pore texture analysis for implanted lightweight hernia mesh identification, with the intention to offer instrumental evidence for the design of larger clinical studies in the future. The improved performance and low cost of ABUS will likely fuel the rapid and broad dissemination of ABUS as an implanted lightweight hernia mesh imaging modality.

Results

a. In vitro study

The ABUS imaging comparisons of four tested meshes are shown in Fig. 4. As an example, the three orthogonal plan views of ABUS imaging of the Ultrapro™

Mesh box are shown in Fig. 5 (a). In comparison, the HHUS imaging result (axial plane) is shown in Fig. 5 (b). The 3D volume rendering results based on ABUS scan data of the UltraproTM Mesh box are shown in Fig. 6, and the results of ABUS imaging of UltraproTM Mesh fragments No. 1 to No. 4 are shown in Fig. 7.

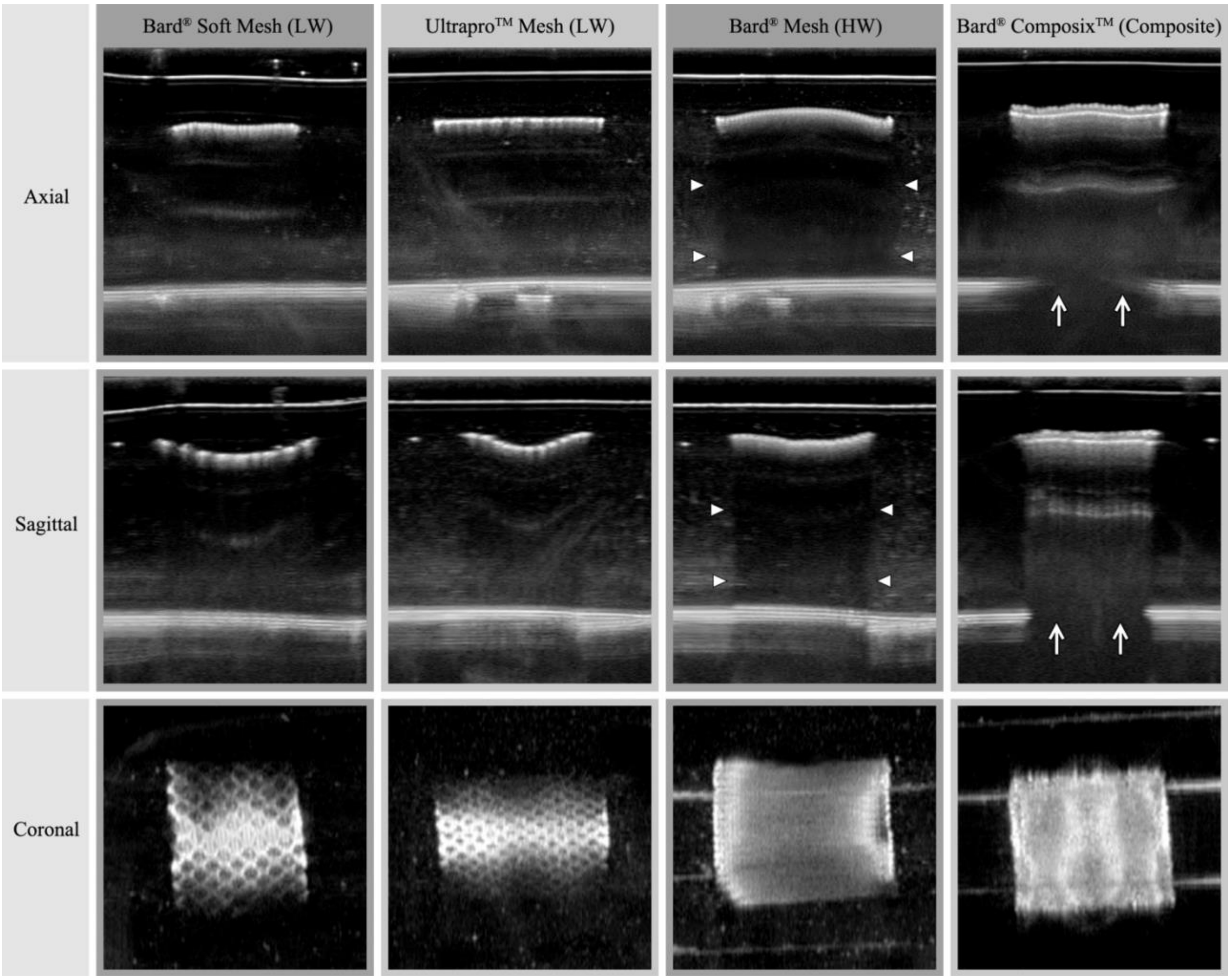

Fig. 4. ABUS imaging comparisons of four tested meshes. The four columns show the Bard® Soft Mesh (LW), the UltraproTM Mesh (LW), the Bard® Mesh (HW), and the Bard® ComposixTM Mesh (Composite) in three orthogonal views, respectively. Note that both LW Bard® Soft and LW UltraproTM meshes are shown in the coronal plane with distinct pore texture. The HW Bard® mesh is shown in sectional views (axial and sagittal views) with posterior acoustic shadowing (arrowheads). The Composite Bard® ComposixTM mesh is shown in sectional views (axial and sagittal views) with badly posterior acoustic shadowing, and the bottom of the plastic container has been unable to observe by ultrasonography (arrows).

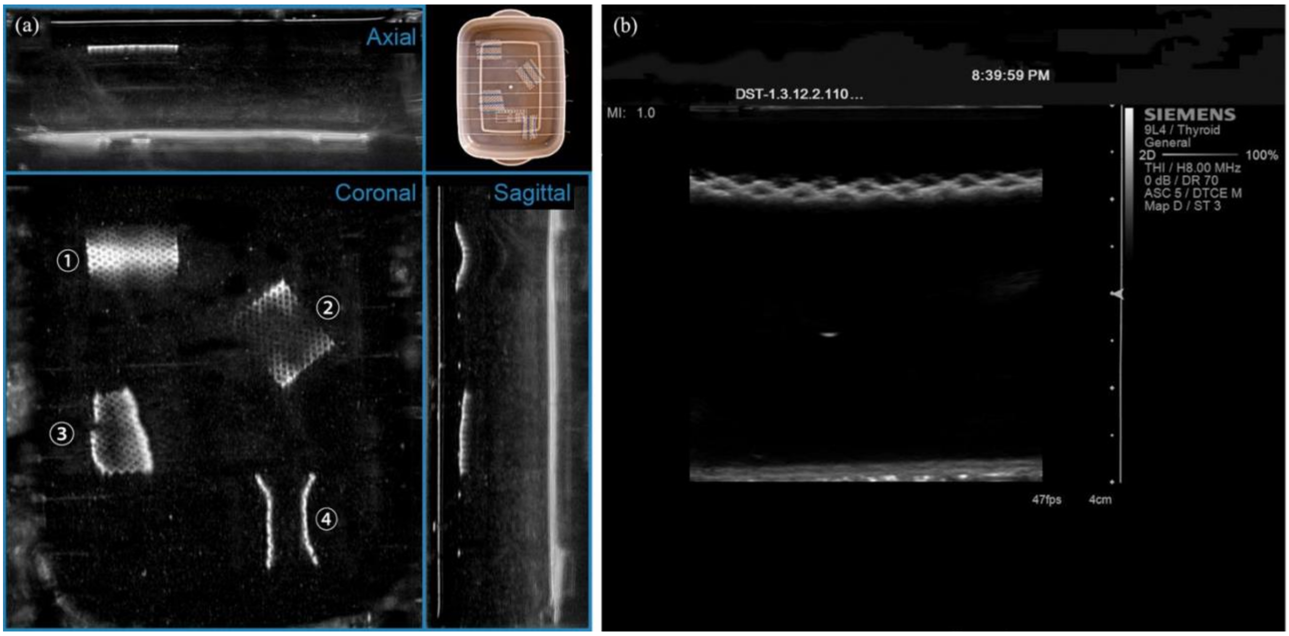

Fig. 5. (a) Three orthogonal plan views of ABUS imaging of the Ultrapro™ Mesh box, while (b) is HHUS imaging result (axial plane). Note that fragment No. ① is parallel to the horizontal plane, fragment No. ② is rotated a certain angle in the horizontal plane, fragment No. ③ is rotated a certain space angle in the depth direction of the horizontal plane, and fragment No. ④ is curved to represent the shrinkage of the mesh. Note that the fragments No. ①-④ are used to simulate the mesh spatial variation that may occur after implantation.

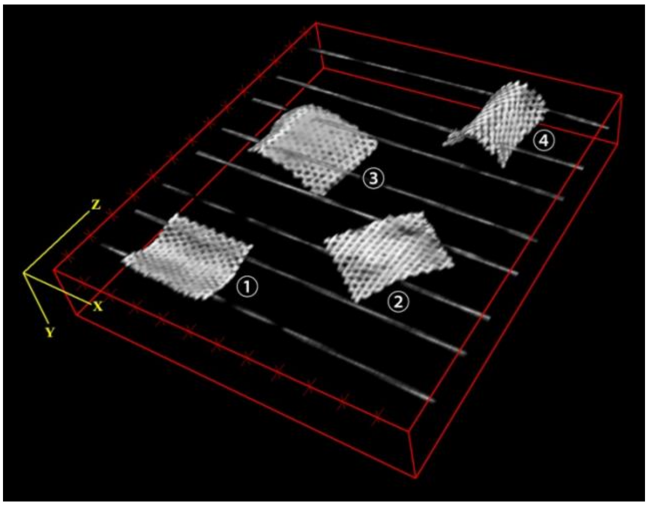

Fig. 6 The 3D volume rendering results based on ABUS scan data of the Ultrapro™ Mesh box.

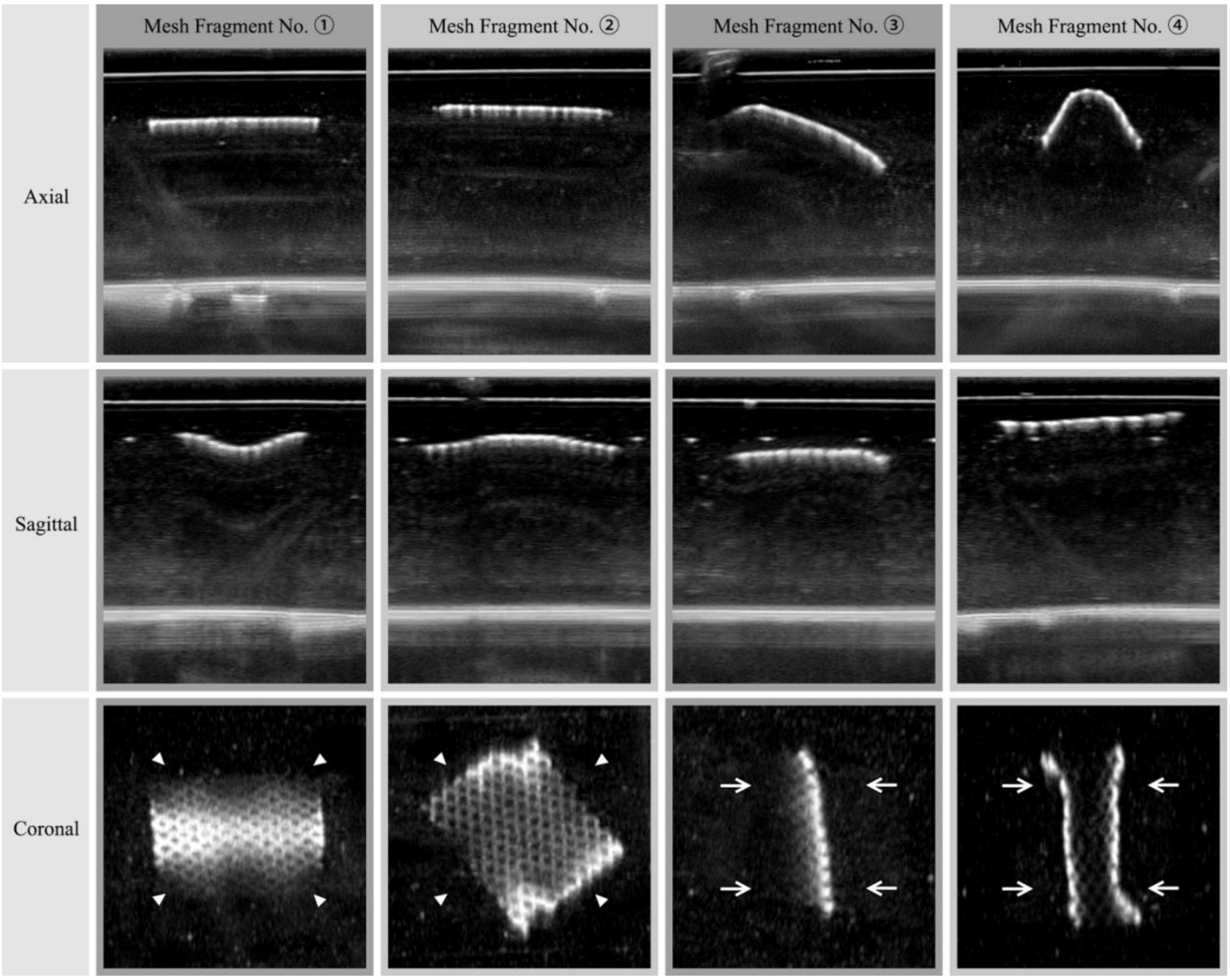

Fig. 7 The results of ABUS imaging of UltraproTM Mesh (LW) with four mesh fragments. Note that fragment No. ① is parallel to the horizontal plane, fragment No. ② is rotated a certain angle in the horizontal plane, fragment No. ③ is rotated a certain space angle in the depth direction of the horizontal plane, and fragment No. ④ is curved to represent the shrinkage of the mesh. Note that the fragments No. ①-④ are used to simulate the mesh spatial variation that may occur after implantation.

b. In vivo study

The calculation results of the inter-class distance for all 40 pore texture features are shown in Fig. 8. The distinction rate between fascia and mesh is directly proportional to the size of parameter values of inter-class distance.

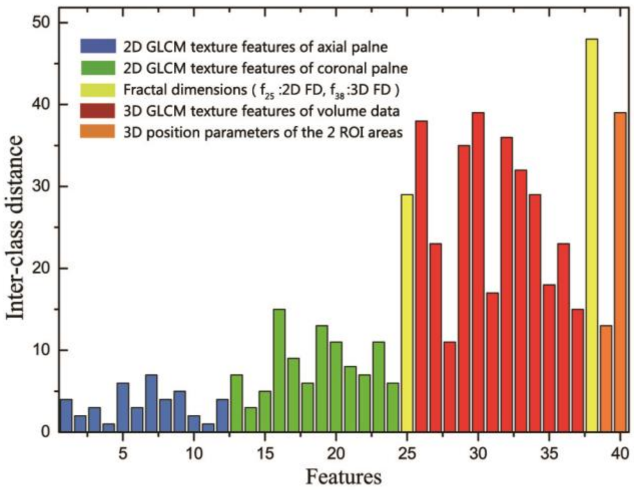

Fig. 8. The inter-class distance results of all 40 pore texture features.

Discussion

Precise visualization of meshes and their position would greatly aid in hernia recurrence risk assessment and the preoperative planning of salvage repair. However, since LW meshes have very thin thickness and large pore sizes between filaments, conventional 3D imaging techniques such as CT and MRI cannot visualize the LW meshes [1]. Patients sometimes have to undergo a second-look operation for visualizing the mesh implants[3]. An innovative new automated 3D breast ultrasound (ABUS) provides additional diagnostic information from coronal views, which cannot be generated by the 2D ultrasound [18]. The new coronal plane offers superior pore texture visualization, by separating the LW mesh from the fascia tissues. From the Fig. 4, 5, 6 and 7, it can be seen that the imaging results of ABUS for implanted LW meshes are much more visualized and effective in comparison to HHUS. This is due to the high resolution of ABUS imaging, and its unique coronal plane provides additional diagnostic information for us.

Heavyweight (HW) meshes and composite meshes have large thickness and weight, small pore sizes between filaments or even no pore. For this reason, these two types of meshes can be observed by conventional 3D imaging methods (CT and MRI). While in ABUS condition, as shown in Fig. 4, the HW and composite meshes also can be observed by ABUS, the reason is that the conventional HW and composite mesh most commonly appears as a linear hyperechoic interface with posterior acoustic shadowing. This appearance can provide the radiologist the ability to easily see the mesh in axial and sagittal views.

As shown in Fig. 5, the imaging result of HHUS for lightweight mesh is very similar to the axial and sagittal plane of ABUS. However, the scanning area of HHUS is very narrow, and the radiologist needs to manually integrate multiple images. While in ABUS condition, since the ABUS has a wide field of view; thus, it can display the entire abdominal wall area at once without missing any parts and allows the radiologist to perceive the implanted LW mesh easily.

From the Fig. 6 and 7, it can be seen that even if there is a spatial variation after the LW mesh implantation, the unique coronal view of ABUS imaging can be used to provide the spatial variation visualization of implanted LW mesh. As shown in Fig. 6 (The 3D volume rendering results based on ABUS scan data of the UltraproTM Mesh box), the ABUS can clearly observe the appearance of the implanted LW mesh after spatial variation.

In vivo study, Fig. 8 shows the inter-class distance results of all 40 pore texture features. From the blue, green and red strip regions of Fig. 8 we can see that the inter-class distance of 2D axial plane texture features (blue strip regions) are generally smaller than others. The reason is that the fascia and LW mesh are approximately presented as a linear bright strip in axial plane view, with little discrimination. Then, compared with the axial plane, the inter-class distance of 2D coronal plane texture features (green strip regions) are higher. The reason is that the LW mesh presents a unique mesh texture in the coronal plane view and offers superior pore texture visualization. However, due to the mesh may have spatial variation such as the curl and shrinkage after implantation, the contribution of 2D coronal plane texture features to LW mesh and fascia identification is not significant. Finally, the inter-class distance of 3D coronal plane texture features are greatly increased compared with 2D coronal plane. The reason is that the use of 3D pore texture features significantly improved the effectiveness and robustness of the identification method in distinguishing the LW mesh and fascia.

As shown in Fig. 8 (yellow strip regions), since the fractal dimension (FD) feature is more suitable for the analysis of the mesh texture, the inter-class distance of 2D FD and 3D FD features are higher than other inter-class distance of features. The inter-class distance of 3D FD feature reaches the maximum value in the inter-class distance of 40 features, which fully reflects that FD features can effective distinguish LW meshes from fascia.

As shown in Fig. 8 (orange strip regions), firstly, although the four tension-free meshes placement positions were located at a scan depth of 1-3 *cm* and the fascia in this area has a higher probability of occurrence, the effect of feature f_{39} (local feature) based on scanning depth to LW mesh and fascia identification is unsatisfactory. Secondly, for recurrent cases of abdominal wall hernia, the repair location of the original abdominal wall hernia is the high incidence of recurrent hernia, thus, the closer to the hernia sac, the higher occurrence of mesh. Therefore, the feature f_{40} (environmental feature) based on the coronal plane position in the region of interest (ROI) can distinguish the LW mesh and the fascia significantly, and it's inter-class distance ranks the third in the inter-class distance ordering of all 40 features.

The 25 features with the high distinction for fascia and mesh were selected according to the order of inter-class distance from large to small, in order to reduce the feature dimension of subsequent classification recognition, improve classification accuracy and reduce classification working time.

Our results provide compelling evidence that ABUS having the potential to provide more accurate features to characterize pore texture patterns. ABUS can provide a broader view which is more convenient for sonologists to observe the entire mesh at one time. Meanwhile, because ABUS can provide more intuitive and easy understood 3D information, sonologists do not need to reconstruct the spatial structure of 3D LW mesh manually in their mind.

Our study, nevertheless, has certain limitations. The small sample size does not provide sufficient statistical power to connote general applicability of our results and to fully determine the superiority of the 3D versus the 2D pore texture analysis methods. However, since this is the first study to explore the pore texture analysis in ABUS images for implanted lightweight hernia mesh identification, our intention was to evaluate proof-of-concept and demonstrate the instrumental evidence required to initiate the design of large clinical studies in the future. Such larger studies will render the sufficient statistical power required to fully evaluate the potential advantages of ABUS imaging in LW mesh identification.

Conclusions

Although preliminary, our results suggest that the mesh pore texture provided by ABUS in the coronal plane is particularly effective in assessing the presence of implanted lightweight meshes. Compared to HHUS imaging, ABUS having the potential to provide more accurate features to characterize mesh pore texture patterns and ultimately provide more accurate measures for implanted LW mesh identification.

Materials and methods

a. In vitro study

In vitro study, four different flat meshes (Fig. 9) was tested. Table 1 shows the basic descriptive data about the four tested meshes. For each tested mesh, 4 fragments [Fig. 10(a), fragments No. ①-④] were used to simulate the mesh spatial variation that may occur after implantation. First, cotton threads were used to control and fix mesh fragments gesture in a plastic container [Fig. 10(a)]. Then, the plastic container filled with gelatin [Fig. 10(b)]. Finally, HHUS and ABUS imaging were performed separately, and the imaging results were evaluated and compared by 2 experienced board-certified radiologists. Fig. 10(c) shows the experimental equipment of in vitro study.

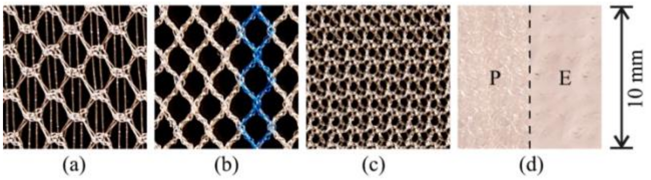

Fig. 9. The top view of four tested meshes. Each photograph shows a 10 mm wide piece of the mesh material. (a) Bard® Soft Mesh (LW); (b) Ultrapro™ Mesh (LW); (c) Bard® Mesh (HW); (d) Bard® Composix™ Mesh (Composite). This composite mesh is constructed of polypropylene mesh on one side (P), bonded with expanded polytetrafluoroethylene (ePTFE) on the other (E).

Table 1. Basic descriptive data about the four tested meshes.

Brand name	Bard® Soft Mesh	Ultrapro™ Mesh	Bard® Mesh	Bard® Composix™ Mesh
Mesh type	Lightweight (LW)	LW	Heavyweight (HW)	Composite
Manufacturer	Bard Davol Inc.	Ethicon, Johnson & Johnson	Bard Davol Inc.	Bard Davol Inc.
Material	polypropylene	polypropylene-poliglecaprone	Polypropylene	polypropylene-ePTFE
Area weight	40 g/m^2	50 g/m^2	102 g/m^2	250 g/m^2
Thickness	0.5 mm	0.5 mm	1.0 mm	2.0 mm
Pore size	3.5 mm	3 mm	1 mm	n/a
Maximum Pressure	n/a	525 mmHg	1650 mmHg	n/a
Instructions by manufacturer	Lightweight mesh designed for open and laparoscopic hernia repair	Partially absorbable lightweight mesh for abdominal wall reinforcement	Conventional polypropylene heavyweight mesh for strong repair	Composite mesh with clinically proven materials to mitigate the risk of visceral adhesion

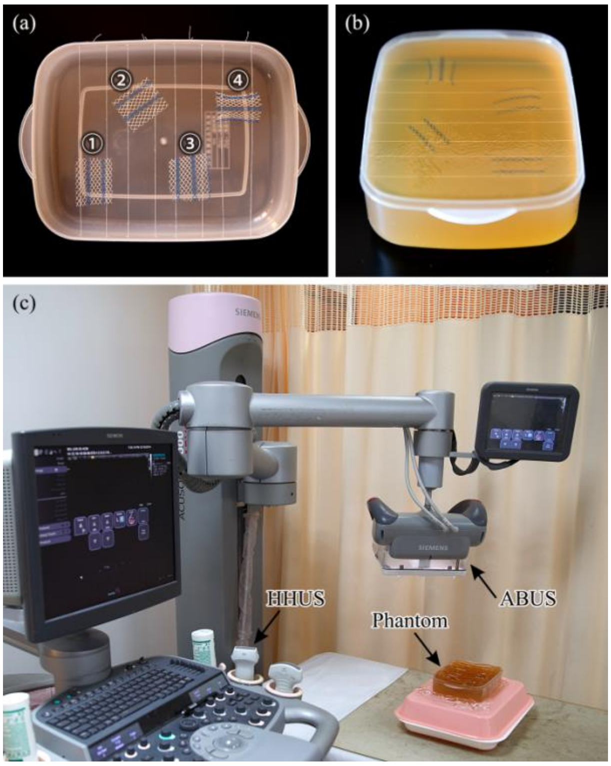

Fig. 10. (a) Plastic container used to hold 4 fragments of the LW Ultrapro™ Mesh, while (b) shows the plastic container filled with gelatin. (c) The experimental equipment of in vitro study. Note that the fragments No. ①-④ are used to simulate the mesh spatial variation that may occur after implantation.

b. In vivo study

1. Study population

From December 2018 to September 2019, 87 patients (56 male and 31 female; age range, 43–79 years; mean age ± SD, 60.6 ± 11.2 years) were recruited for the in vivo study. The study was approved by the Ethics Committee of Huadong Hospital. All patients were volunteers who signed informed consent. The patients were referred to our ultrasound department for specific diagnostic queries, such as erythema, swelling, pain in the hernia region, intensified screening for symptoms suspicious for hernia recurrence, and preoperative diagnosis. All patients underwent HHUS and ABUS examinations in the hernia region. To obtain the evaluation criteria for confirming the lightweight mesh identified with ABUS and HHUS pore texture features, only the patients who subsequently underwent surgery were considered in our study. On the basis of the surgical findings, 38 of these patients (44%) with previously implanted lightweight hernia mesh constituted the case group, and 49 patients (56%) with no implanted lightweight hernia mesh constituted the control group. After anonymization, the HHUS and ABUS dataset was then available for further study.

2. Examination methods (HHUS vs. ABUS)

The HHUS examinations were performed by a radiologist with five years' experience in abdominal wall hernia sonography using an ACUSON S2000 ultrasound system (Siemens Medical Solutions, Mountain View, CA, USA). The patients were placed in the supine position for the examination. The Static 2D images were obtained using a 14L5 linear array transducer at 11 MHz central frequency. Images in axial and sagittal planes that best manifested the central hernia region were stored on an offline workstation for review and analysis.

The ABUS examinations were performed also on Siemens ACUSON S2000 by the same radiologist, but with a 14L5BV linear transducer. The central frequency of transducer varied from 9 to 11 MHz. The frequency was set at 11 MHz for the present study. This transducer is able to capture a volume of 154 × 168 × 60 mm^3 in a single scan. In each scanning, the ABUS generates 318 2D slices with a layer thickness of 0.5 *mm* in axial direction. ABUS examinations were performed with the patients lying in the same position as they were for the HHUS scanning. Before scanning, the radiologist applied appropriate pressure to the transducer to keep the probe closely attached to the central hernia region surface [Fig. 2(a)]. After acquisition, the volume data sets were automatically sent from the ultrasound system to the diagnostic workstation, which enabled comprehensive analysis and manipulation of the 3D data.

3. Image analysis

A region of interest (ROI) was manually segmented from the central hernia region in each image. The physical dimensions of the ROIs were selected to be 10 mm^3 for the ABUS images, and 10 mm^2 for the HHUS images, based on previous suggestions for the average pore size of LW mesh in the literature [13]. Corresponding to these physical dimensions, 143 ×143 ×19 pixel ROIs at 0.07 *mm*/pixel in-plane resolution and 0.53 *mm* tomographic slice spacing were segmented from all the reconstructed ABUS images; matching 143×143 pixel ROIs at 0.07 *mm*/pixel resolution were segmented in the corresponding HHUS images of the same central hernia region. Examples of such ROIs are shown in Fig. 11.

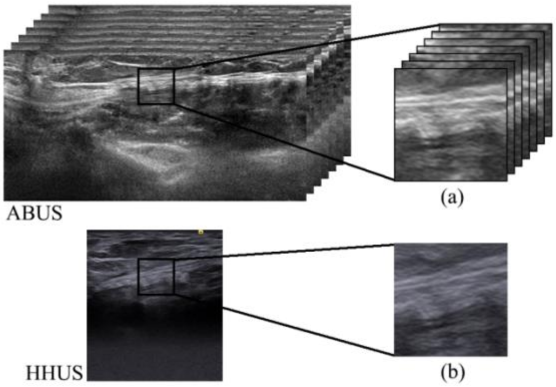

Fig. 11. An illustrative example of (a) a 3D ROI segmented from a reconstructed automated 3-D breast ultrasound (ABUS) image and (b) the corresponding 2D ROI from the hand-held ultrasound (HHUS) of the same central hernia region.

To characterize the pore texture pattern, texture features of energy, contrast, correlation, variance, homogeneity, sum average, entropy, autocorrelation, dissimilarity, cluster shade ,cluster prominence, maximum probability and fractal dimension (FD) were estimated from all the ABUS and HHUS ROIs. These texture features were originally defined for the analysis of 2D images. While texture analysis method have been widely implemented for the analysis of 2D medical images [24], the available techniques for 3D pore texture analysis are currently limited. Recently YAHIA Samah et al. demonstrated an efficient method for the analysis of textures in the 3-dimensional space [25]. In our study, two approaches were implemented for pore texture analysis in the 3D reconstructed ABUS images: tomographic (2D) and volumetric (3D) texture analysis [26].

4. Tomographic (2D) texture analysis

The gray level co-occurrence matrix (GLCM) is one of the most known texture analysis operators. Based on measuring texture features, this operator computes the order of co-occurrence of pixels pairs at a certain direction and distance [25]. Haralick et al. defined gray level co-occurrence matrix [27]. We give a uniform definition of gray-level co-occurrence matrix for both 2D and 3D data. Consider an image (either 2D or 3D) which is rebound to G gray levels where G is a positive integer. The difference of spatial locations of two pixel points (2D) or two voxels (3D) in an image can be described by a displacement vector D. For an image of G gray levels, the $G \times G$ gray level co-occurrence matrix P_{ij} for a displacement vector D is defined as follows. The entry (i, j) of P_{ij} is the number of occurrence of voxel-pair of gray levels i and j whose spatial locations are a vector D apart. When normalized by the total counts, the entry (i, j) of P_{ij}, denoted as $P(i, j)$, represents the probability of occurrence of voxel pair of gray levels i and j whose spatial locations are a vector D apart. In this definition, the co-occurrence matrix P_{ij} is a function of the displacement vector D which can be decomposed into a norm-1 distance d and a direction. Thus, P_{ij} describes distributions of certain spatial patterns of scale d in a certain direction.[28]

In 2D images, the difference of spatial locations of two pixel points can be described by displacement vector $D(\varphi, d)$, where φ is the angle of two pixel points and the coordinate axis, and d is the distance between two pixel points. For 2D images, the possible spatial relations of a pair of pixels are shown in Fig.12. Given a certain distance d, there are eight neighboring pixel pairs in four independent directions: horizontal, vertical, diagonal and anti-diagonal (corresponding to 0°, 90°, 45° and 135°, respectively).

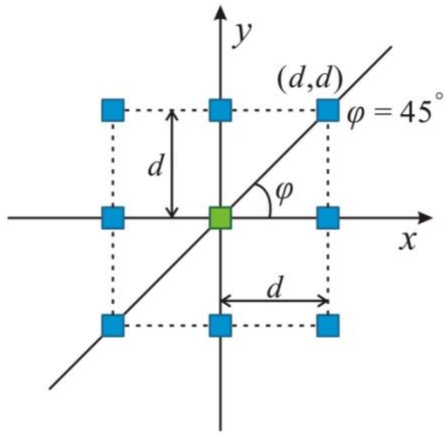

Fig. 12. Spatial relations of a pair of pixels in 2D. For a particular pixel (green), it has eight neighboring pixels (blue) of norm-1 distance d in 4 independent directions.

Haralick et al. proposed 14 texture features, twelve of these features were selected in our study, including energy (f_1),contrast (f_2),correlation (f_3),variance(f_4), homogeneity (f_5),sum average (f_6),entropy (f_7),autocorrelation (f_8),dissimilarity (f_9),cluster shade (f_{10}),cluster prominence (f_{11}),maximum probability (f_{12}). The co-occurrence frequencies were calculated symmetrically in the four independent directions around each pixel using a displacement vector $D = (dx, dy)$ along x and y dimensions, where $dx = dy = 1$ pixel offset [26]. The texture features calculated in each of these four independent directions were averaged to create a single measure that was used in our experiments.

$$f_1 = \sum_i \sum_j P(i,j)^2 \tag{1}$$

$$f_2 = \sum_{n=0}^{N_g-1} n^2 \left\{ \sum_{i=1}^{N_g} \sum_{j=1}^{N_g} P(i,j) \| i-j \| = n \right\} \tag{2}$$

$$f_3 = \frac{\sum_i \sum_j (i \cdot j) P(i,j) - \mu_x \mu_y}{\sigma_x \sigma_y} \tag{3}$$

$$f_4 = \sum_i \sum_j (i - \mu)^2 P(i,j) \tag{4}$$

$$f_5 = \sum_i \sum_j \frac{P(i,j)}{1 + (i-j)^2} \tag{5}$$

$$f_6 = \sum_{i=2}^{2N_g} i P_{x+y}(i) \tag{6}$$

$$f_7 = -\sum_i \sum_j P(i,j) \log(P(i,j)) \tag{7}$$

$$f_8 = \sum_i \sum_j (i \cdot j) P(i,j) \tag{8}$$

$$f_9 = \sum_i \sum_j |i - j| \cdot P(i,j) \tag{9}$$

$$f_{10} = \sum_i \sum_j (i + j - \mu_x - \mu_y)^3 P(i,j) \tag{10}$$

$$f_{11} = \sum_i \sum_j (i + j - \mu_x - \mu_y)^4 P(i,j) \tag{11}$$

$$f_{12} = \underset{i,j}{MAX}\, P(i,j) \tag{12}$$

Where $P(i,j)$ is the normalized gray level co-occurrence matrix. The average value and standard deviation of the rows and columns of matrix are:

$$\mu_x = \sum_i \sum_j i P(i,j) \tag{13}$$

$$\mu_y = \sum_i \sum_j j P(i,j) \tag{14}$$

$$\sigma_x = \sum_i \sum_j (i-\mu_x)^2 P(i,j) \tag{15}$$

$$\sigma_y = \sum_i \sum_j (j-\mu_y)^2 P(i,j) \tag{16}$$

Fractal dimension (FD) was estimated based on the power spectrum of the Fourier transform of the image [26]. The 2D Discrete Fourier Transform (DFT) was performed using the Fast Fourier Transform (FFT) algorithm as:

$$\mathrm{F(u,v)} = \sum_{\mathrm{m=0}}^{\mathrm{M\text{-}1}} \sum_{\mathrm{n=0}}^{\mathrm{N\text{-}1}} \mathrm{I(m,n)} e^{-j(2\pi/M)um} e^{-j(2\pi/N)vn}, \quad \mu = 0,1,\ldots,M-1; \nu = 0,1,\ldots,N-1 \tag{17}$$

Where I is the 2D image region of size (M,N), and μ and v are the spatial frequencies in the x and y directions. The power spectral density P was estimated from $F(\mu,v)$ as:

$$P(u,\ v) = |F(u,v)|^2 \tag{18}$$

Finally, in order to compute the 2D FD, P was averaged along the radial slices direction across the FFT frequency domain. The frequency space was uniformly divided in 24 directions, with each direction uniformly sampled at 30 points along the radial component. The least-squares-fit of the $log(P_f)$ versus $log(f)$ was estimated, where $f = \sqrt{u^2 + v^2}$ denotes the radial frequency. The 2D FD is related to the slope β of the logarithmic curve in the following form:

$$FD = \frac{3D_T + 2 - \beta}{2} = \frac{8-\beta}{2} \tag{19}$$

Where D_T is the topological dimension, and is equal to $D_T = 2$ for a 2D image.

5. Volumetric (3D) texture analysis

When calculating gray-level pore texture statistics, traditional 2D texture descriptors were extended to 3D by considering a 3D neighborhood of voxels (i.e., volume elements) instead of a 2D neighborhood of pixels.

In 3D images, the difference of spatial locations of two voxels can be described by a displacement vector $D(\varphi, \theta, d)$,where φ and θ is the azimuth and the zenith angle respectively, and d is the distance between two voxels (Fig. 13 left). As shown in Fig. 13, there are totally 26 neighboring voxel-pairs in 13 independent directions. Here, it is still selected to extract the same 12 3D GLCM texture features as in 2D GLCM. The 3D displacement vector $D = (d_x, d_y, d_z)$ was defined around each voxel along the x, y and z dimensions, where $d_x = d_y = d_z = 1$ is the voxel offset. Texture features were calculated in each of these 13 directions and they were averaged to create a single measure that was used in our experiments.

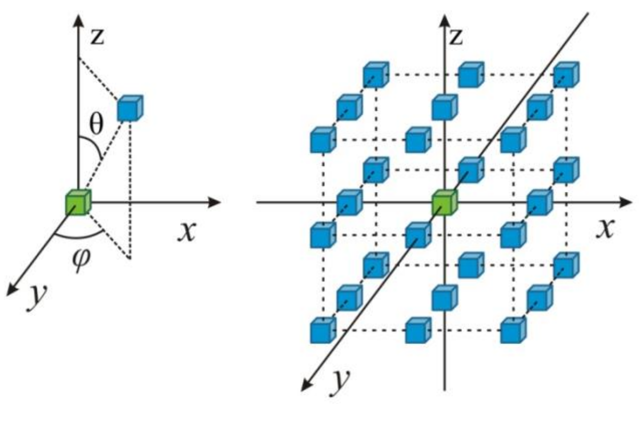

Fig. 13. Spatial relations of a pair of voxels in 3D. For a particular voxel (green), it has 26 neighbors (blue) of norm-1 distance d in 13 independent directions.

Fractal dimension (FD) was estimated based on the power spectrum of the 3D Fourier transform of the image. FFT algorithm was used to perform 3D DFT for the entire 3D ROI area:

$$F(u,v,w) = \sum_{m=0}^{M-1}\sum_{n=0}^{N-1}\sum_{k=0}^{K-1} I(m,n,k)e^{-j(2\pi/M)um}e^{-j(2\pi/N)vn}e^{-j(2\pi/K)wk} \quad (20)$$

Where I is the 3D image region of size (M,N,K) ,and u ,v and w are the spatial frequencies in the x, y and z directions respectively. The power spectral density P was estimated as:

$$P(u,v,w) = \left|F(u,v,w)\right|^2 \quad (21)$$

Finally, in order to calculate 3D FD, P was averaged along the radial sector direction across the 3D FFT frequency domain. The frequency space was uniformly divided in 24 azimuth directions and 12 zenith angles, with each direction uniformly sampled at 30 points along the radial component. The least-squares-fit of the $log(P_f)$ versus $log(f)$ was estimated, where $f = \sqrt{u^2 + v^2 + w^2}$ represents the radial frequency, 2D FD was related to the slope β of the logarithmic curve in the following form:

$$FD_{3D} = \frac{3D_T + 2 - \beta}{2} = \frac{11 - \beta}{2} \quad (22)$$

Where D_T is the topological dimension, and is equal to $D_T = 3$ for 3D image.

6. Pore texture analysis for implanted lightweight hernia mesh identification

We performed pore texture analysis on the 2D ROIs of HHUS and 3D ROIs of ABUS. First, all 40 pore texture features that mentioned earlier were extracted for each ROI region. The extracted pore texture features include 25 2D features, 13 3D features, one local feature (f_{39}) based on the scanning depth of ROI region and one environmental feature (f_{40}) based on the relationship between ROI region and hernia sac location. Then, the inter-class distance of each pore texture was calculated. Finally, the differences of inter-class distance were analyzed for selecting more discriminative features.

List of abbreviations

2D, 3D: two, three dimensional

ABUS: automated 3D breast ultrasound

CT: computed tomography

DFT: discrete fourier transform

FD: fractal dimension

FFT: fast fourier transform

GLCM: gray level co-occurrence matrix

HHUS: hand-held ultrasound

HW: Heavyweight

LW: Lightweight

MRI: magnetic resonance imaging

ROI: region of interest

Declarations

Ethics approval and consent to participate

The study was approved by the Ethics Committee of Huadong Hospital. All patients were volunteers who signed informed consent.

Consent for publication

Not applicable.

Availability of data and material

The datasets used and/or analysed during the current study are available from the corresponding author on reasonable request.

Competing interests

The authors declare that they have no competing interests.

Funding

This work was supported by the Grant (61661050, 61561050) from the Natural Science Foundation of China and Priority Union Foundation of Yunnan Provincial Science and Technology Department and Kunming Medical University (2018FE001(-143)).

Authors' contributions

JY implemented the draft and analyzed the data. HL and JW suggested the proposed algorithm. YW and YZ was responsible for theoretical guidance. LS, YC, DX and LC implemented the experiments. All authors read and approved the final manuscript.

Acknowledgements

Not applicable.

Authors' information

Affiliations

Department of Electronic Engineering, Yunnan University, Kunming, 650091, China
Jiting Yang, Haiyan Li, Jun Wu, Dan Xu & Yufeng Zhang

Department of Gastrointestinal and Hernia Surgery, The First Affiliated Hospital of Kunming Medical University, Kunming, 650032, China
Liang Sun

Department of Electronic Engineering, Fudan University, Shanghai, 200433, China
Yuanyuan Wang

Department of Ultrasound, Huadong Hospital, Fudan University, Shanghai, 200040, China
Yue Chen & Lin Chen

Corresponding authors

Correspondence to Jun Wu & Liang Sun.

References

1. Rakic S, LeBlanc KA. The radiologic appearance of prosthetic materials used in hernia repair and a recommended classification. American Journal of Roentgenology. 2013; 201:1180-1183.
2. Carter PR, LeBlanc KA, Hausmann MG, Whitaker JM, Rhynes VK, Kleinpeter KP*, et al*. Does expanded polytetrafluoroethylene mesh really shrink after laparoscopic ventral hernia repair? Hernia : the journal of hernias and abdominal wall surgery. 2012; 16:321-325.
3. Kuehnert N, Kraemer NA, Otto J, Donker HC, Slabu I, Baumann M*, et al*. In vivo MRI visualization of mesh shrinkage using surgical implants loaded with superparamagnetic iron oxides. Surgical endoscopy. 2012; 26:1468-1475.
4. Jin J, Rosen MJ. Laparoscopic versus open ventral hernia repair. Surgical Clinics of North America. 2008; 88:1083-1100.
5. Pham TD, Le DTP, Xu J, Nguyen DT, Martindale RG, Deveney CW. Personalized identification of abdominal wall hernia meshes on computed tomography. Computer methods and programs in biomedicine. 2014; 113:153-161.
6. Falagas ME, Kasiakou SK. Mesh-related infections after hernia repair surgery. Clinical Microbiology and Infection. 2005; 11:3-8.
7. Cassar K, Munro A. Surgical treatment of incisional hernia. British Journal of Surgery. 2002; 89:534-545.
8. Jamadar DA, Jacobson JA, Girish G, Balin J, Brandon CJ, Caoili EM*, et al*. Abdominal wall hernia mesh repair: sonography of mesh and common complications. J Ultras Med. 2008; 27:907-917.
9. Burger JW, Luijendijk RW, Hop WC, Halm JA, Verdaasdonk EG, Jeekel J. Long-term follow-up of a randomized controlled trial of suture versus mesh repair of incisional hernia. Annals of surgery. 2004; 240:578-583; discussion 583-575.
10. Schumpelick V, Klinge U, Junge K, Stumpf M. Incisional abdominal hernia: the open mesh repair. Langenbecks Archives of Surgery. 2004; 389:1-5.
11. Park AE, Roth JS, Kavic SM. Abdominal wall hernia. Current problems in surgery. 2006; 43:326-375.
12. Girish G, Caoili EM, Pandya A, Dong Q, Franz MG, Morag Y*, et al*. Usefulness of the twinkling artifact in identifying implanted mesh after inguinal hernia repair. J Ultras Med. 2011; 30:1059-1065.
13. Cobb WS, Kercher KW, Heniford BT. The argument for lightweight polypropylene mesh in hernia repair. Surgical innovation. 2005; 12:63-69.
14. Cobb WS, Burns JM, Peindl RD, Carbonell AM, Matthews BD, Kercher KW*, et al*. Textile analysis of heavy weight, mid-weight, and light weight polypropylene mesh in a porcine ventral hernia model. Journal of Surgical Research. 2006; 136:1-7.
15. Aguirre DA, Santosa AC, Casola G, Sirlin CB. Abdominal wall hernias: imaging features, complications, and diagnostic pitfalls at multi-detector row CT. Radiographics : a review publication of the Radiological Society of North America, Inc. 2005; 25:1501-1520.
16. Jain N, Goyal N, Mukherjee K, Kamath S. Ultrasound of the abdominal wall: what lies beneath? Clinical radiology. 2013; 68:85-93.

17. Wu J, Wang Y, Yu J, Chen Y, Pang Y, Diao X, *et al*. Identification of implanted mesh after incisional hernia repair using an automated breast volume scanner. J Ultras Med. 2015; 34:1071-1081.
18. Lin X, Wang J, Han F, Fu J, Li A. Analysis of eighty-one cases with breast lesions using automated breast volume scanner and comparison with handheld ultrasound. European journal of radiology. 2012; 81:873-878.
19. Wojcinski S, Farrokh A, Hille U, Wiskirchen J, Gyapong S, Soliman AA, *et al*. The automated breast volume scanner (ABVS): initial experiences in lesion detection compared with conventional handheld b-mode ultrasound: a pilot study of 50 cases. International journal of women's health. 2011; 3:337-346.
20. Golatta M, Franz D, Harcos A, Junkermann H, Rauch G, Scharf A, *et al*. Interobserver reliability of automated breast volume scanner (ABVS) interpretation and agreement of ABVS findings with hand held breast ultrasound (HHUS), mammography and pathology results. European journal of radiology. 2013; 82:e332-336.
21. Wu J, Wang YY, Yu JH, Shi XL, Zhang JH, Chen Y, *et al*. Intelligent speckle reducing anisotropic diffusion algorithm for automated 3-D ultrasound images. J Opt Soc Am A. 2015; 32:248-257.
22. Diao X, Chen Y, Qiu Z, Pang Y, Zhan J, Chen L. Diagnostic value of an automated breast volume scanner for abdominal hernias. J Ultras Med. 2014; 33:39-46.
23. Fang L, Chen L, Wang WP, Chen Y, Pang Y, Qiu ZY, *et al*. Diagnostic value of automated 3D ultrasound for incisional hernia. Ultrasound in Medicine and Biology. 2014; 40:1966-1972.
24. Waugh SA, Purdie CA, Jordan LB, Vinnicombe S, Lerski RA, Martin P, *et al*. Magnetic resonance imaging texture analysis classification of primary breast cancer. 2016; 26:322-330.
25. Samah Y, Yassine Bs, Naceur AM: Analysis of 3D Textures Based on Features Extraction. In 2018 15th International Multi-Conference on Systems, Signals & Devices (SSD); 19-22 March 2018. 2018:1216-1220.
26. Kontos D, Bakic PR, Carton AK, Troxel AB, Conant EF, Maidment AD. Parenchymal texture analysis in digital breast tomosynthesis for breast cancer risk estimation: a preliminary study. Academic radiology. 2009; 16:283-298.
27. Haralick RM, Shanmugam K, Dinstein IH. Textural features for image classification. IEEE Transactions on Systems, Man and Cybernetics. 1973; SMC-3:610-621.
28. Chen W, Giger ML, Li H, Bick U, Newstead GM. Volumetric texture analysis of breast lesions on contrast-enhanced magnetic resonance images. Magnetic resonance in medicine : official journal of the Society of Magnetic Resonance in Medicine / Society of Magnetic Resonance in Medicine. 2007; 58:562-571.

Figures

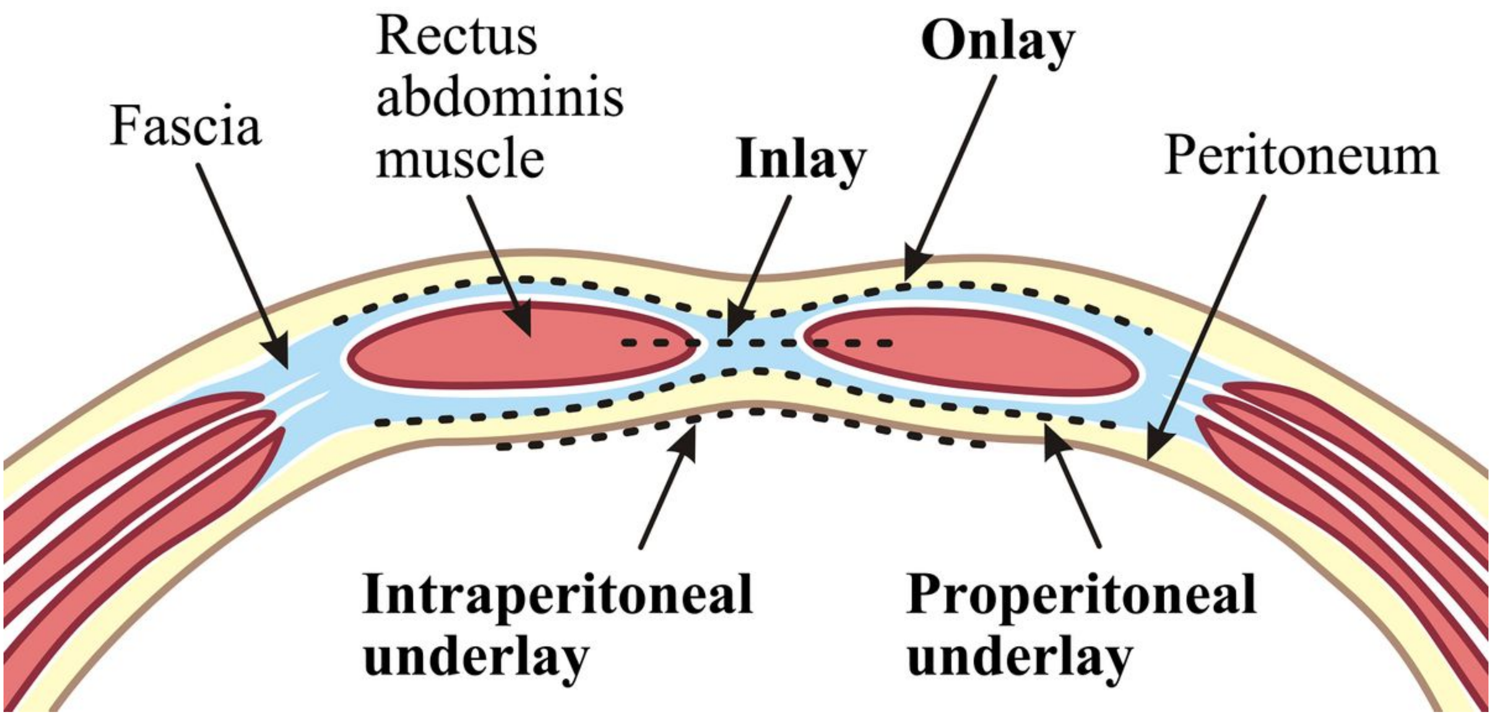

Figure 1

Anterior abdominal wall in cross section above the arcuate line. The mesh (black dashed lines) may be anterior to the abdominal wall fascia (Onlay), be adjacent to the fascial edges (Inlay), in the preperitoneal space between the fascia and the peritoneum (Properitoneal underlay), or be attached to the peritoneum in an intraperitoneal position (Intraperitoneal underlay).

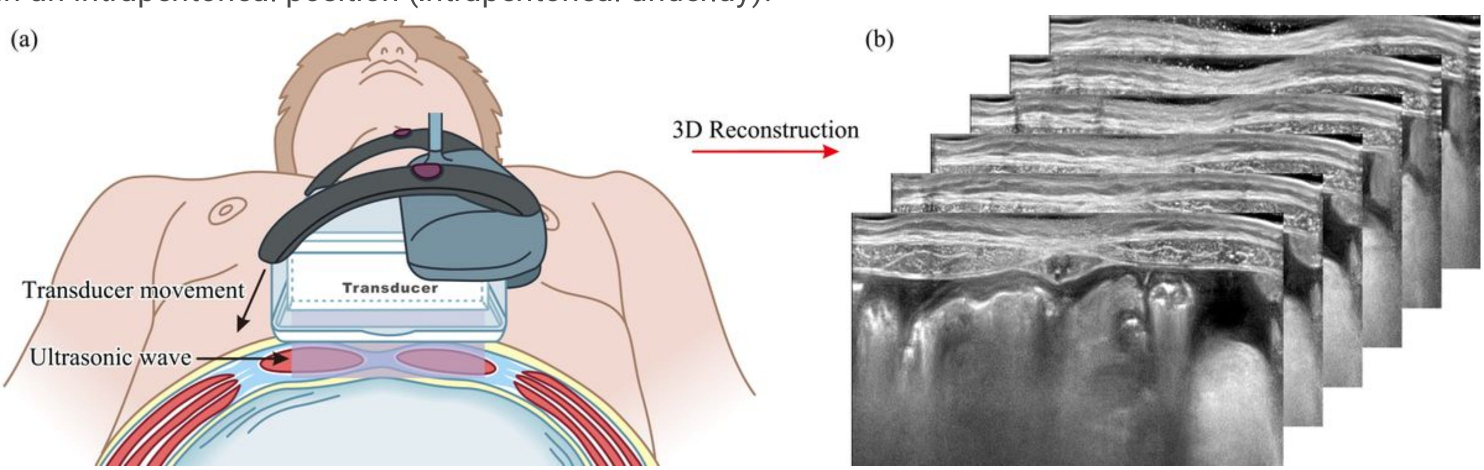

Figure 2

An illustrative example of (a) automated 3D breast ultrasound (ABUS) acquisition geometry with (b) the reconstructed tomographic anterior abdominal wall image.

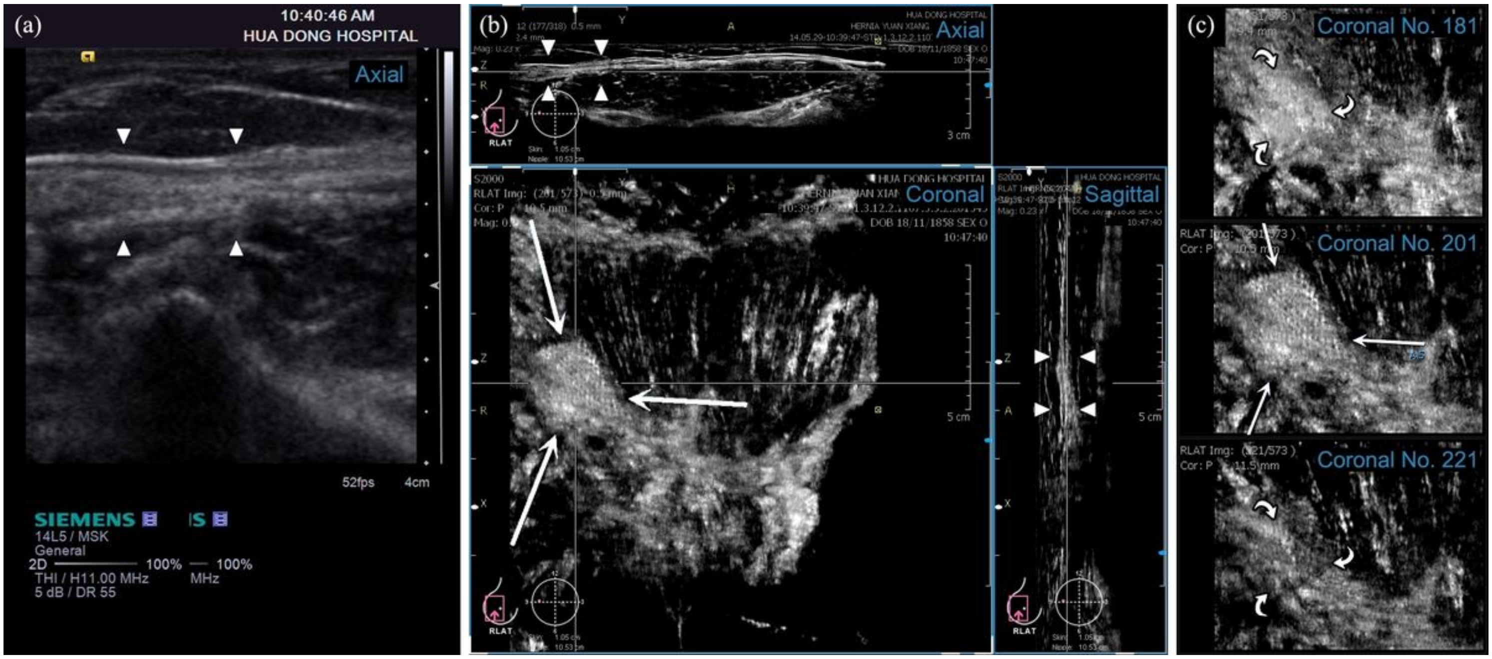

Figure 3

Differences of texture features in (a) the axial view of HHUS, (b) the three orthogonal views of ABUS and (c) coronal multislice views of ABUS for the same LW mesh. Note that the texture features of HHUS images reflect mixed properties of LW mesh overlapping fascia tissues. Therefore, it is difficult to identify the LW mesh itself separate from the fascia tissues that surround it (arrowheads). However, the new coronal plane of ABUS offers superior pore texture visualization, by separating the LW mesh (arrows) from the fascia (curved arrows) tissues.

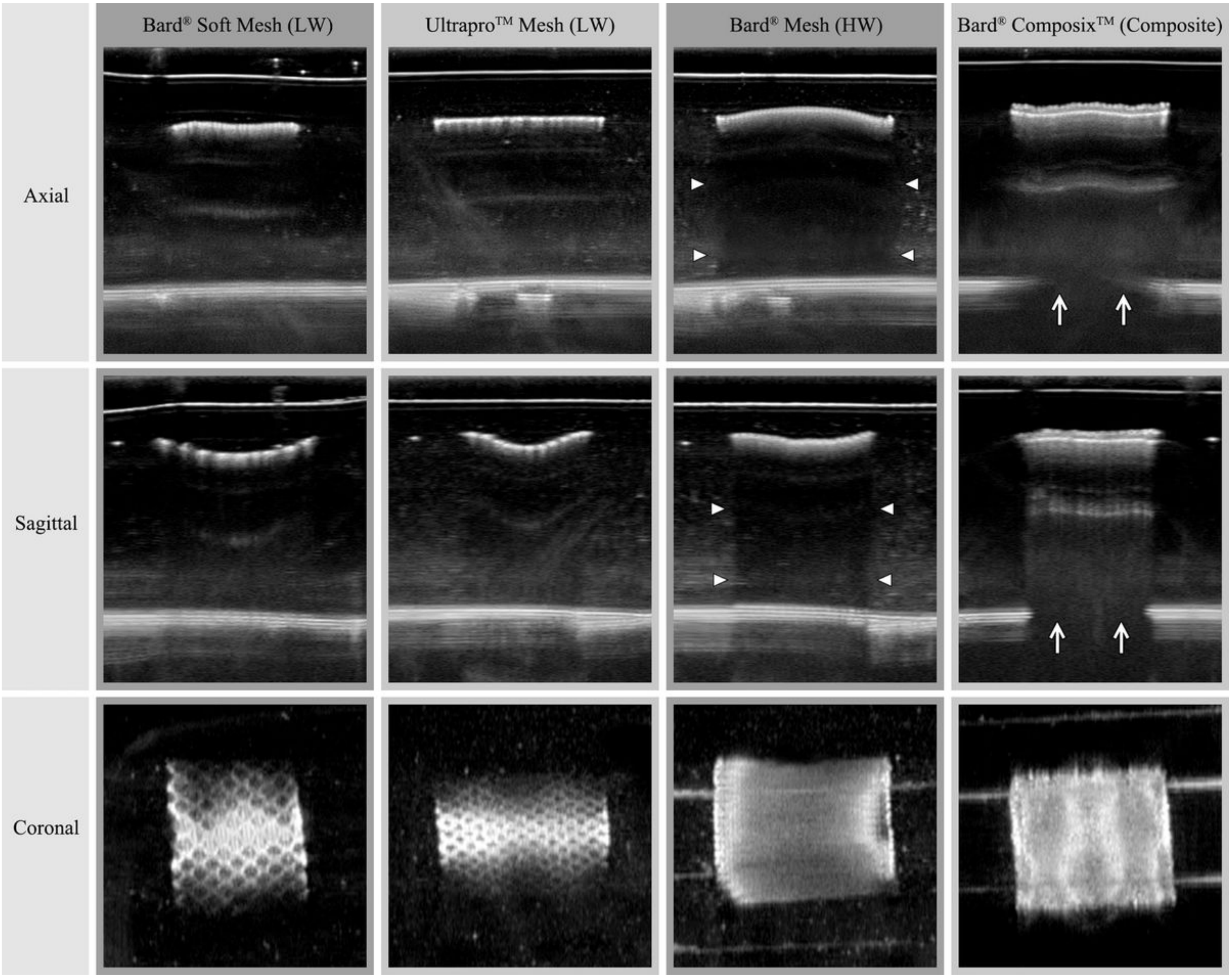

Figure 4

ABUS imaging comparisons of four tested meshes. The four columns show the Bard® Soft Mesh (LW), the UltraproTM Mesh (LW), the Bard® Mesh (HW), and the Bard® ComposixTM Mesh (Composite) in three orthogonal views, respectively. Note that both LW Bard® Soft and LW UltraproTM meshes are shown in the coronal plane with distinct pore texture. The HW Bard® mesh is shown in sectional views (axial and sagittal views) with posterior acoustic shadowing (arrowheads). The Composite Bard® ComposixTM mesh is shown in sectional views (axial and sagittal views) with badly posterior acoustic shadowing, and the bottom of the plastic container has been unable to observe by ultrasonography (arrows).

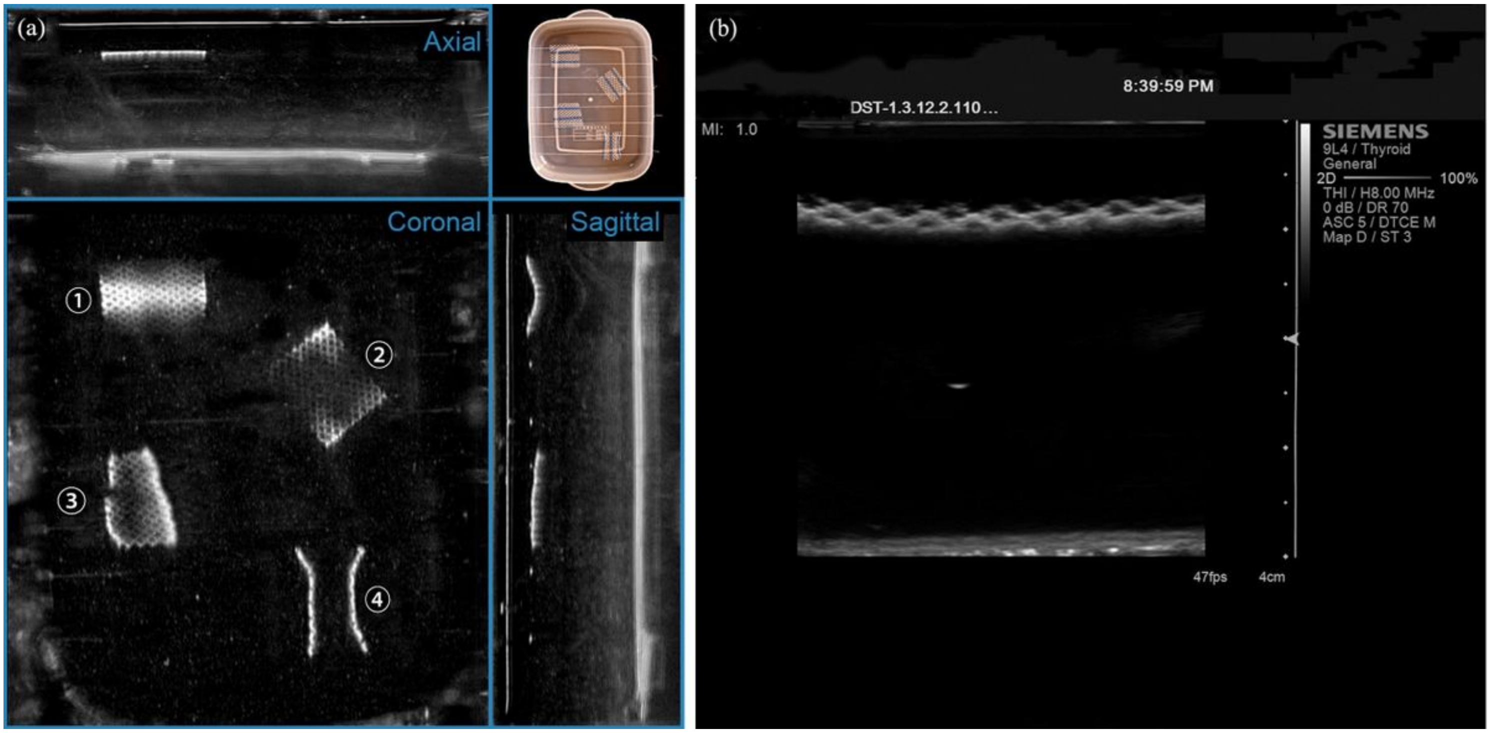

Figure 5

(a) Three orthogonal plan views of ABUS imaging of the UltraproTM Mesh box, while (b) is HHUS imaging result (axial plane). Note that fragment No. 1 is parallel to the horizontal plane, fragment No. 2 is rotated a certain angle in the horizontal plane, fragment No. 3 is rotated a certain space angle in the depth direction of the horizontal plane, and fragment No. 4 is curved to represent the shrinkage of the mesh. Note that the fragments No. 1-4 are used to simulate the mesh spatial variation that may occur after implantation.

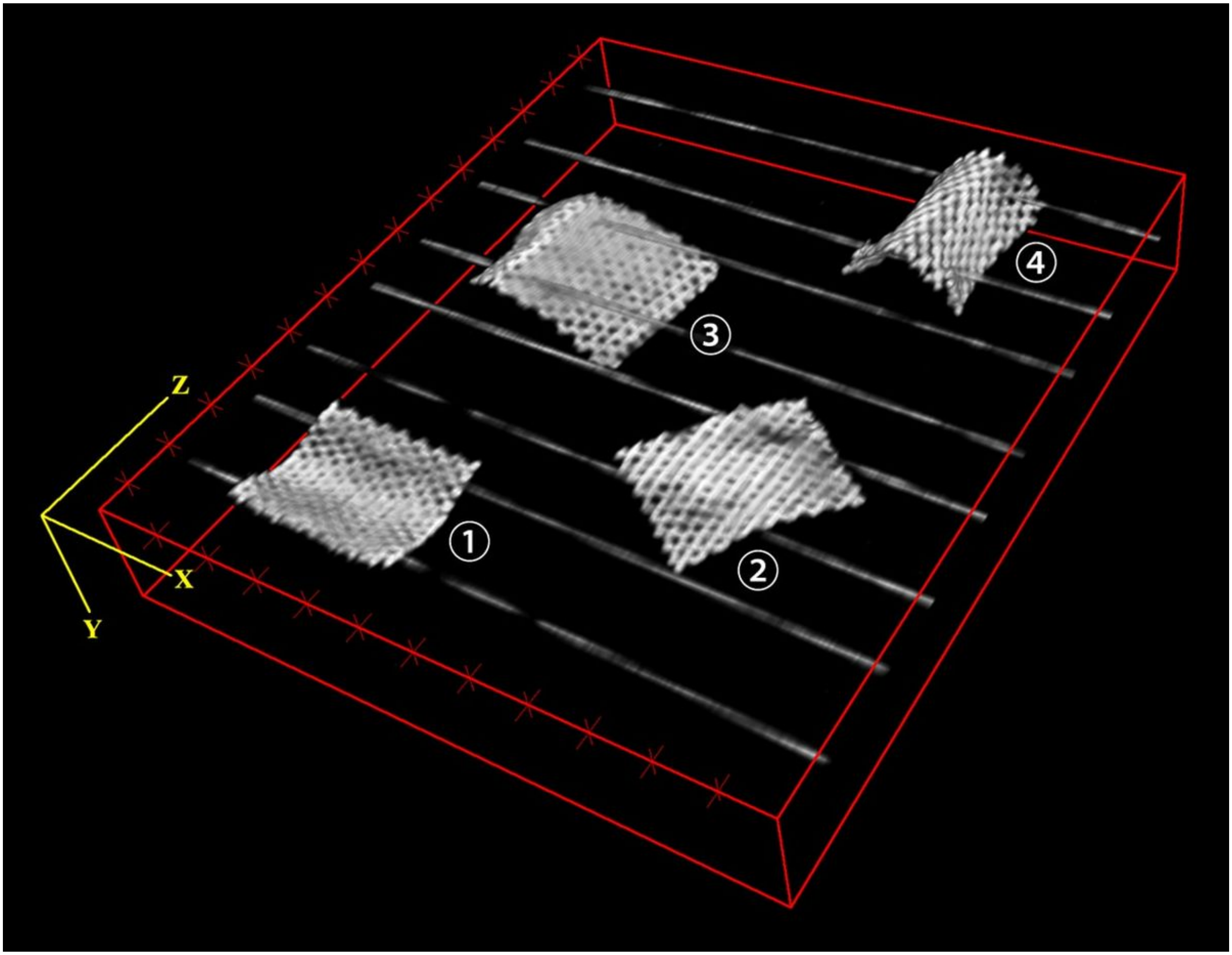

Figure 6

The 3D volume rendering results based on ABUS scan data of the UltraproTM Mesh box.

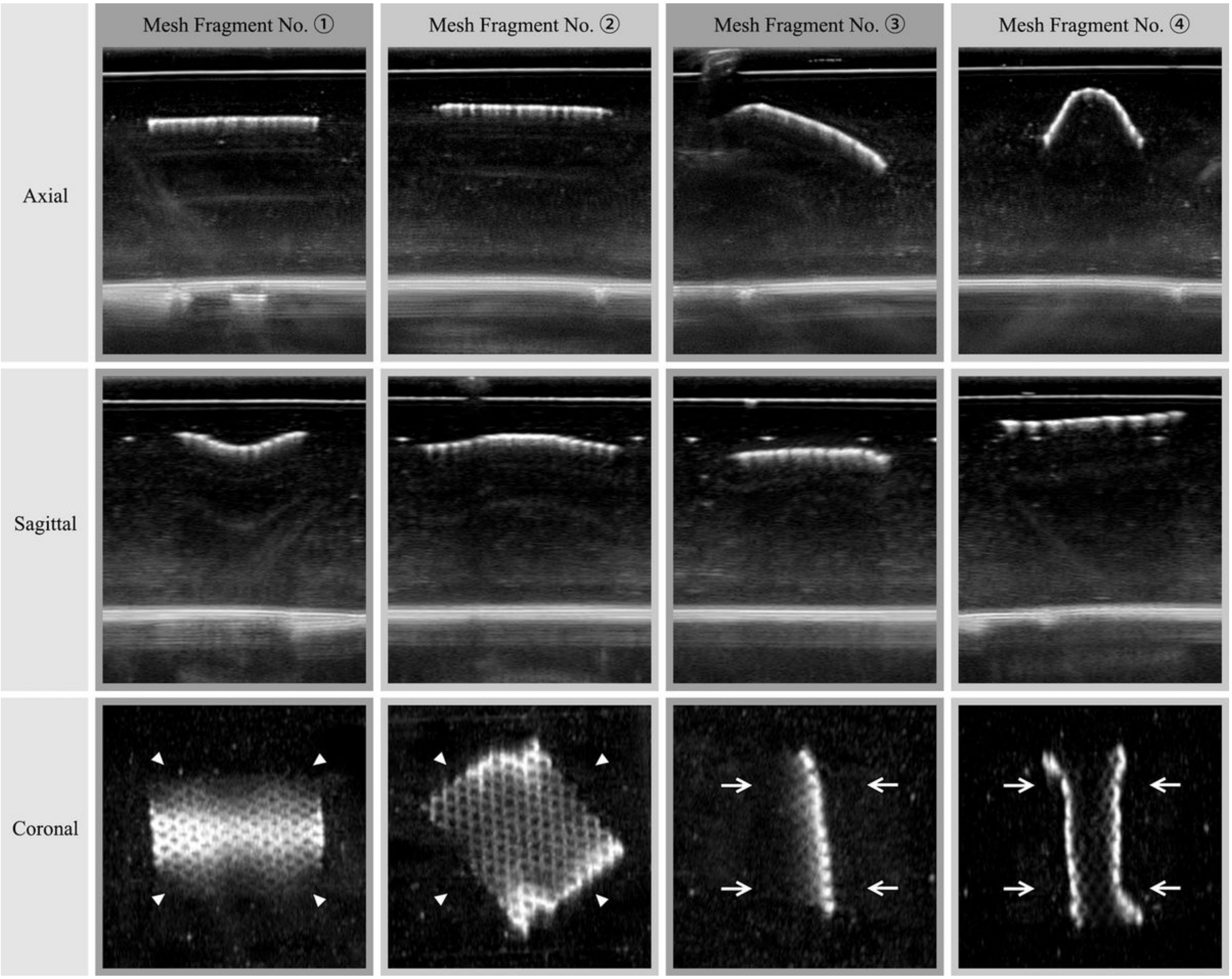

Figure 7

The results of ABUS imaging of UltraproTM Mesh (LW) with four mesh fragments. Note that fragment No. 1 is parallel to the horizontal plane, fragment No. 2 is rotated a certain angle in the horizontal plane, fragment No. 3 is rotated a certain space angle in the depth direction of the horizontal plane, and fragment No. 4 is curved to represent the shrinkage of the mesh. Note that the fragments No. 1-4 are used to simulate the mesh spatial variation that may occur after implantation.

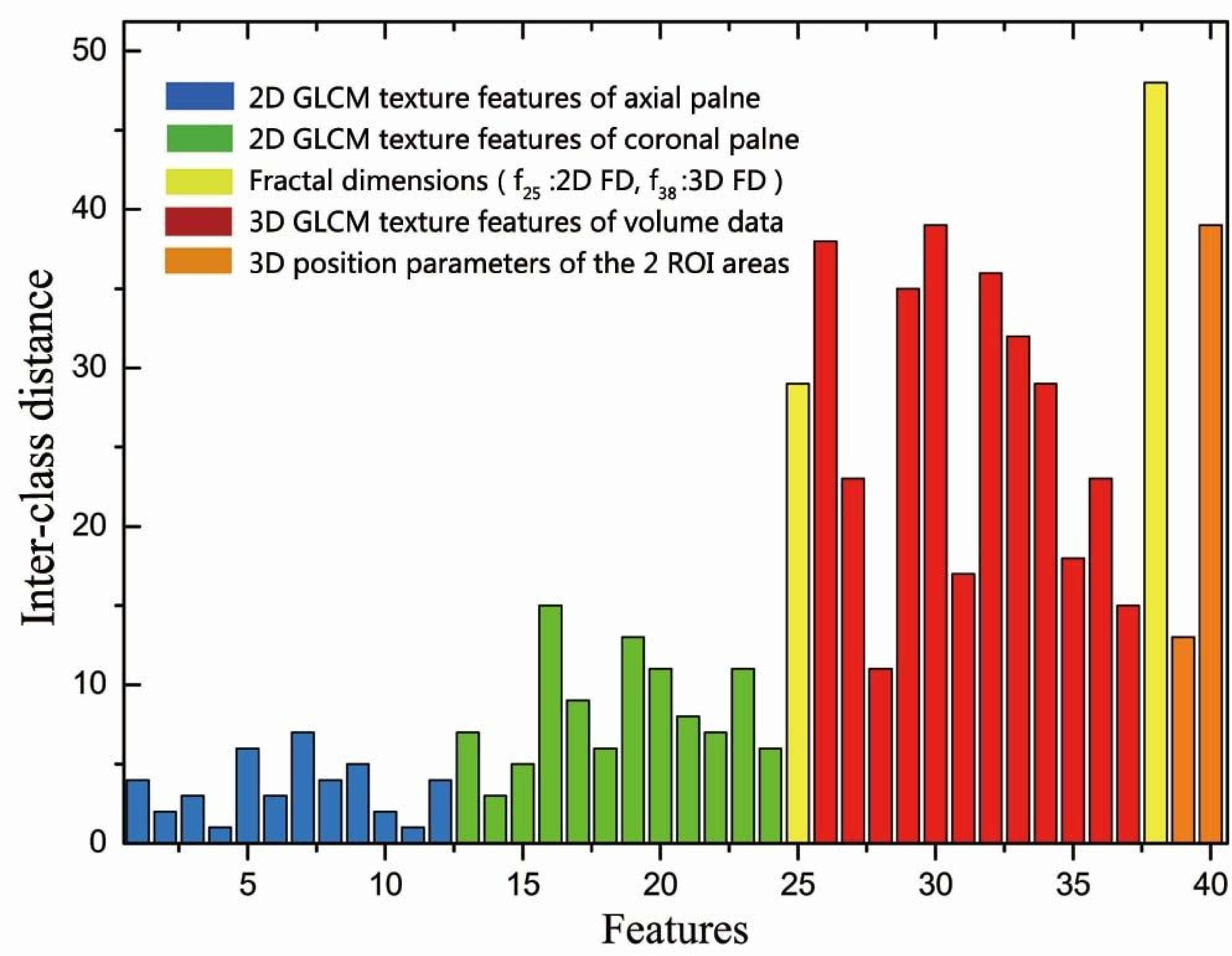

Figure 8

The inter-class distance results of all 40 pore texture features.

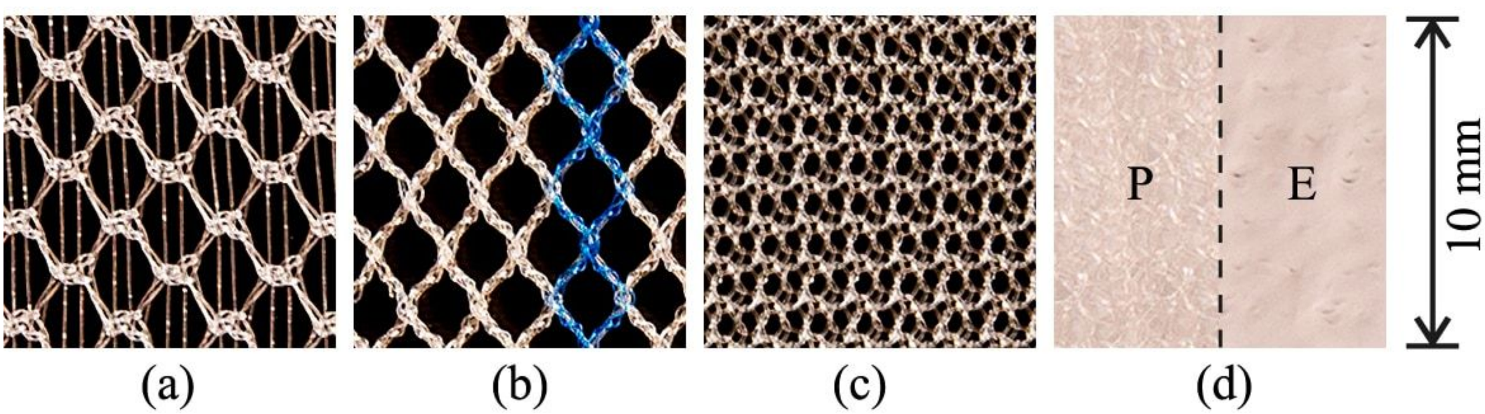

Figure 9

The top view of four tested meshes. Each photograph shows a 10 mm wide piece of the mesh material. (a) Bard® Soft Mesh (LW); (b) UltraproTM Mesh (LW); (c) Bard® Mesh (HW); (d) Bard® ComposixTM Mesh (Composite). This composite mesh is constructed of polypropylene mesh on one side (P), bonded with expanded polytetrafluoroethylene (ePTFE) on the other (E).

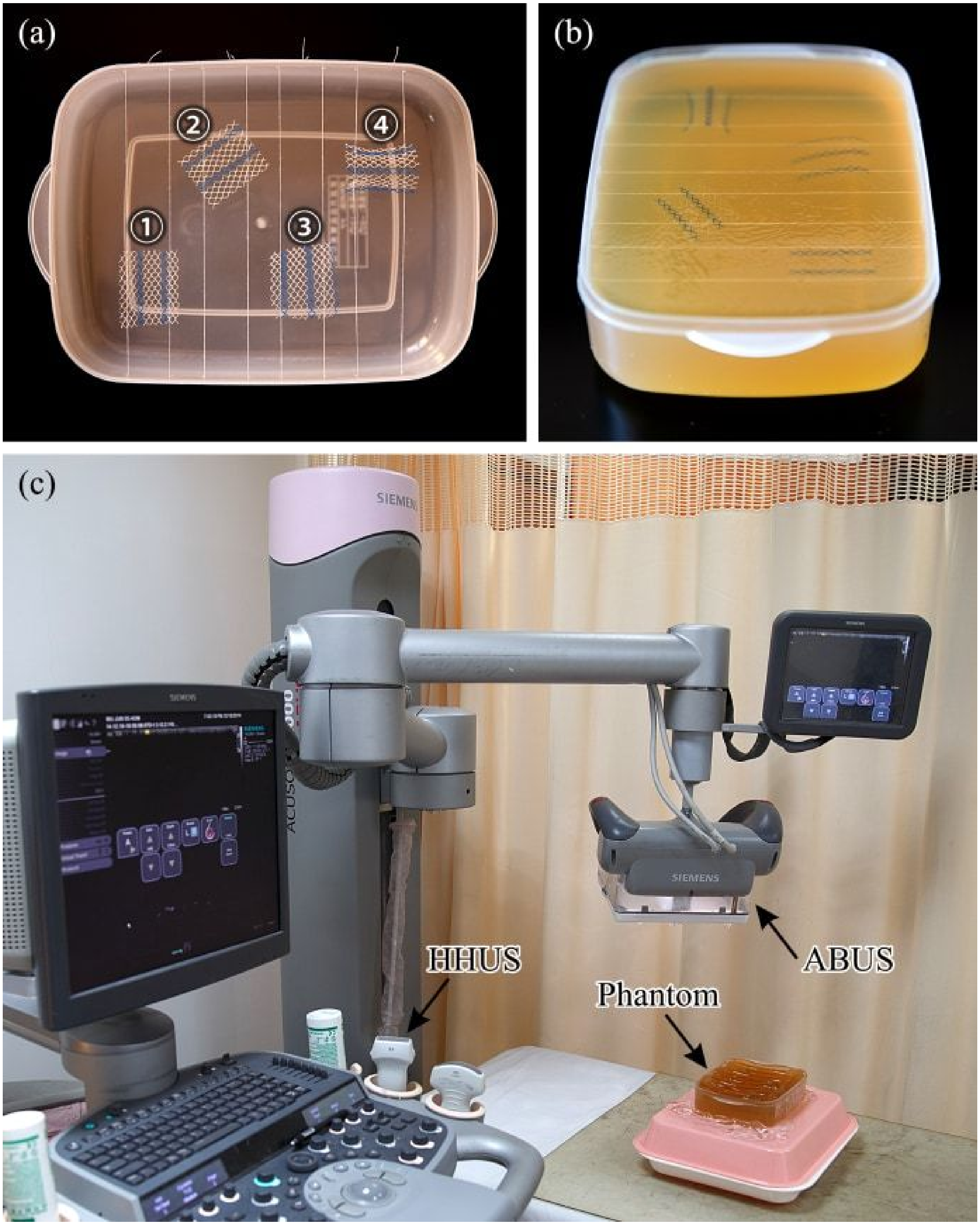

Figure 10

(a) Plastic container used to hold 4 fragments of the LW UltraproTM Mesh, while (b) shows the plastic container filled with gelatin. (c) The experimental equipment of in vitro study. Note that the fragments No. 1-4 are used to simulate the mesh spatial variation that may occur after implantation.

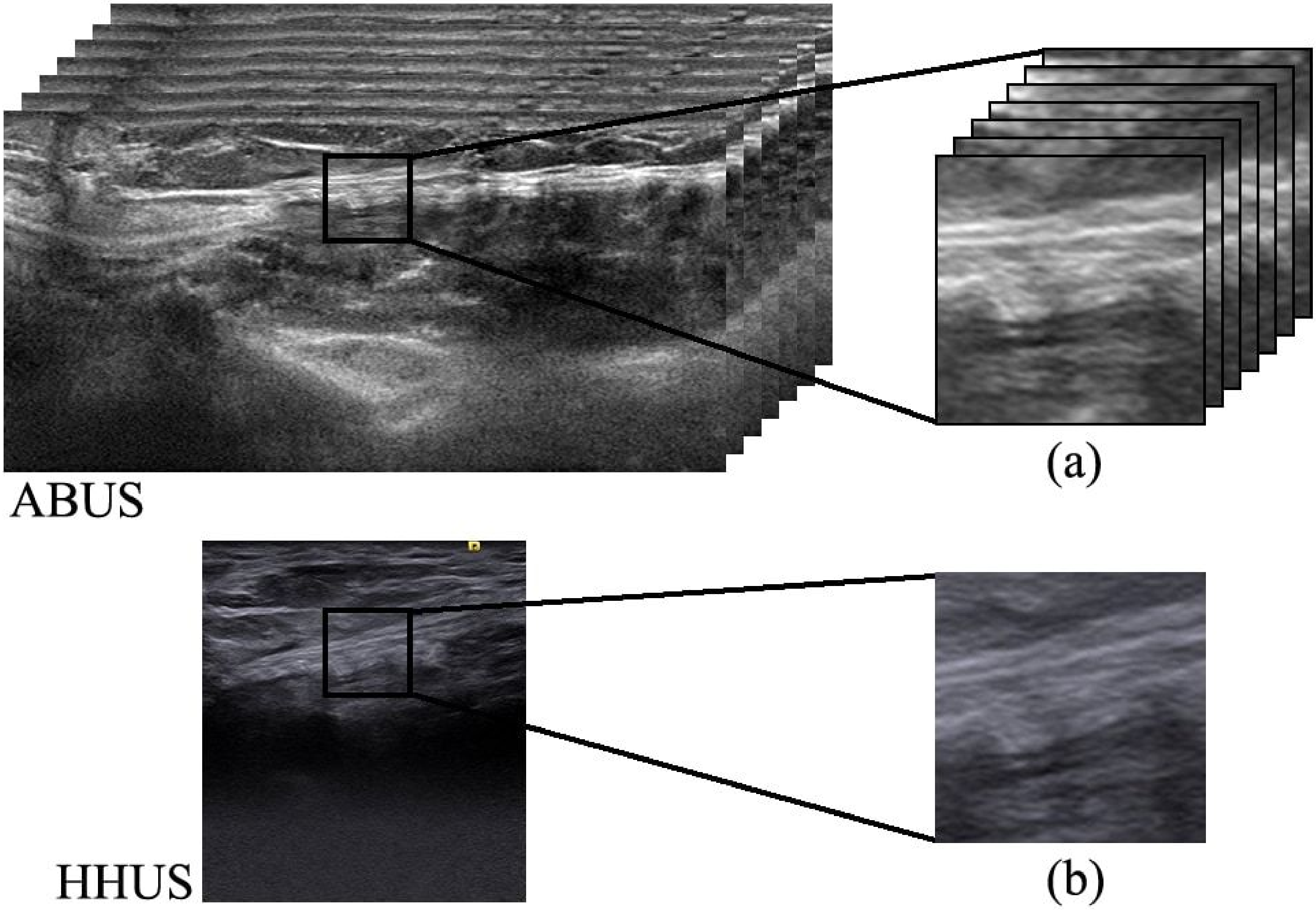

Figure 11

An illustrative example of (a) a 3D ROI segmented from a reconstructed automated 3-D breast ultrasound (ABUS) image and (b) the corresponding 2D ROI from the hand-held ultrasound (HHUS) of the same central hernia region.

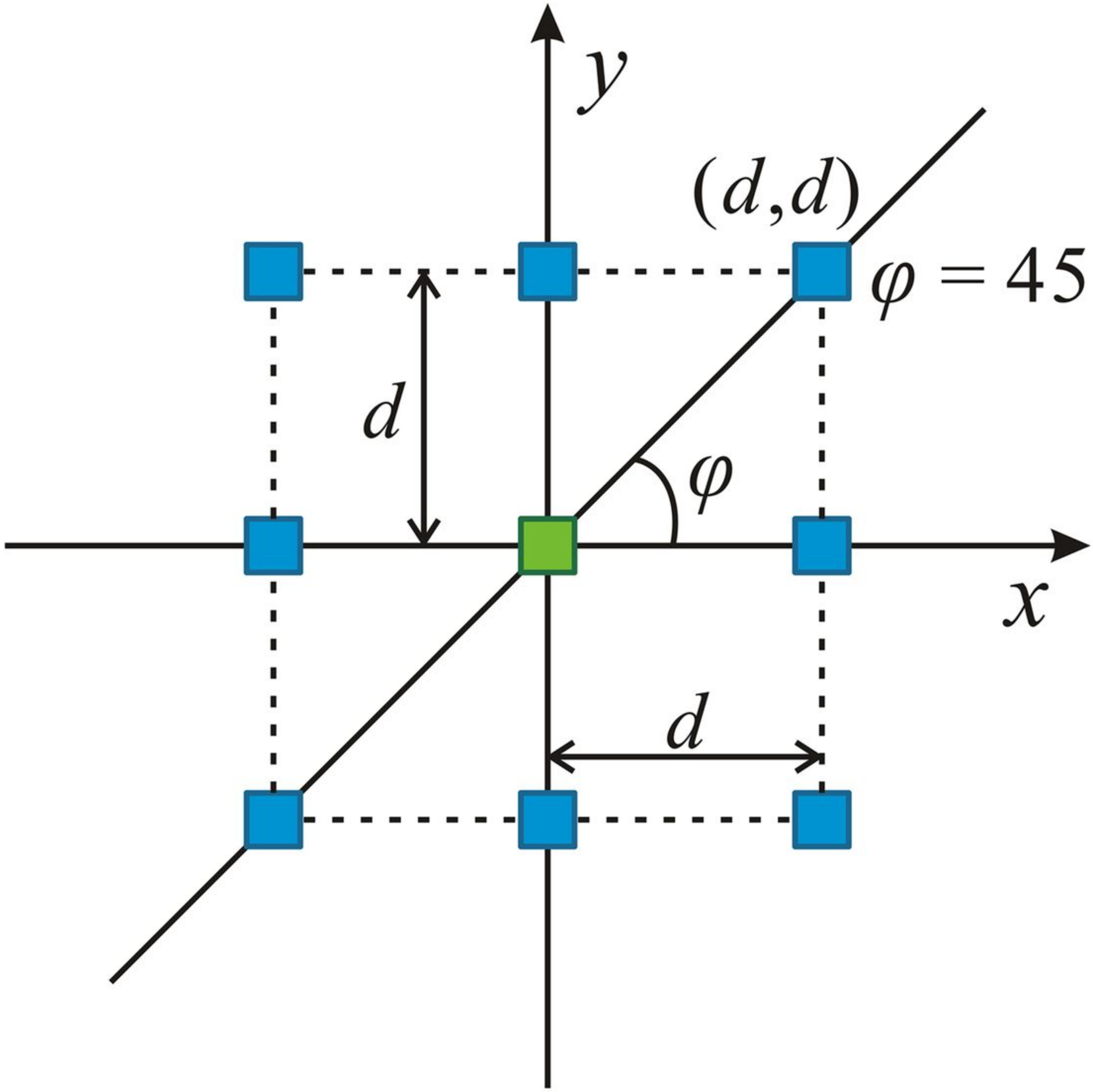

Figure 12

Spatial relations of a pair of pixels in 2D. For a particular pixel (green), it has eight neighboring pixels (blue) of norm-1 distance d in 4 independent directions.

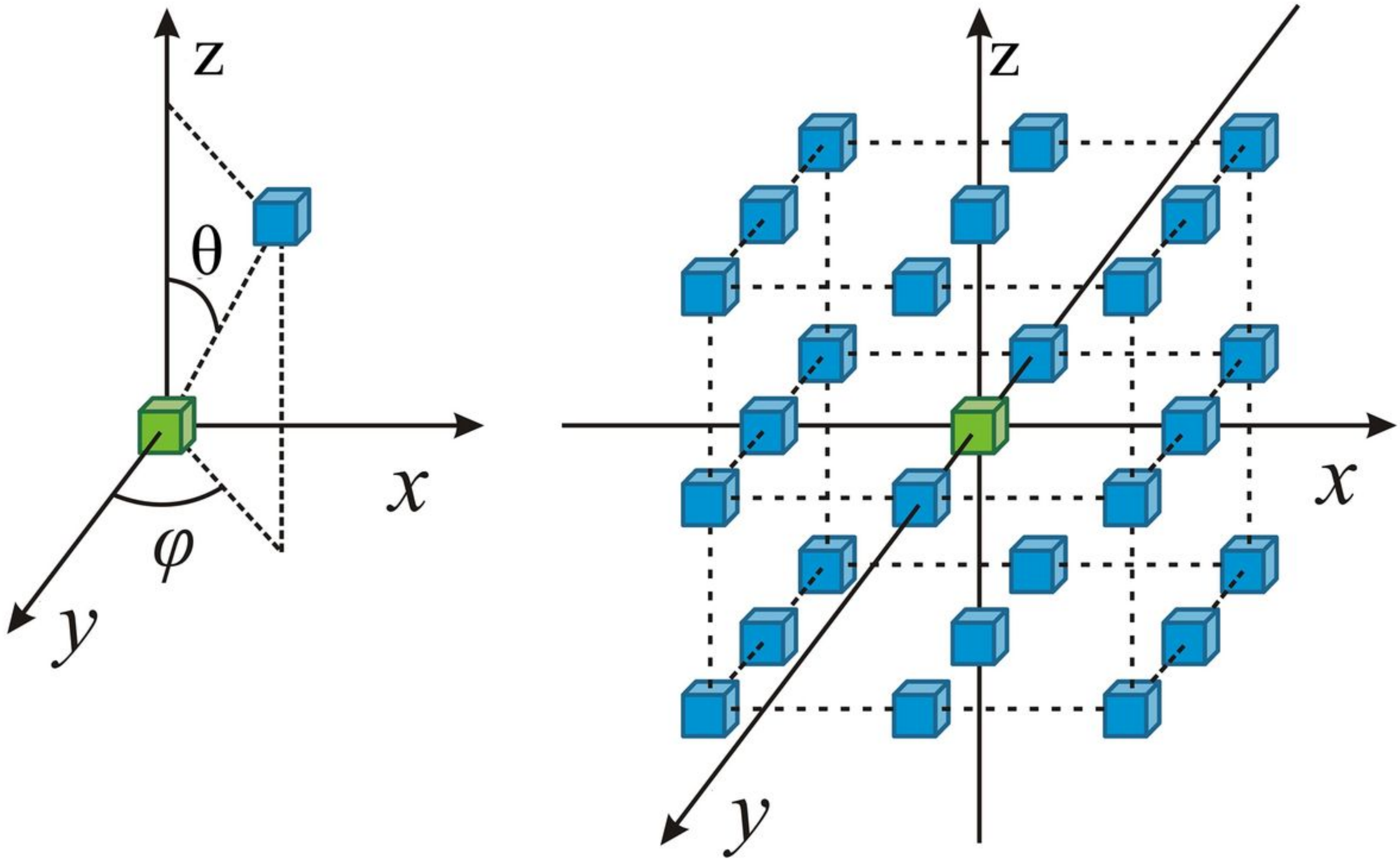

Figure 13

. Spatial relations of a pair of voxels in 3D. For a particular voxel (green), it has 26 neighbors (blue) of norm-1 distance d in 13 independent directions.